ARTICLE IN PRESS

Journal of Atmospheric and Solar-Terrestrial Physics ∎ (∎∎∎∎) ∎∎∎–∎∎∎

Contents lists available at ScienceDirect

Journal of Atmospheric and Solar-Terrestrial Physics

journal homepage: www.elsevier.com/locate/jastp

Solar connections of geoeffective magnetic structures

N. Gopalswamy *

NASA Goddard Space Flight Center, Greenbelt, MD, USA

ARTICLE INFO

Article history:
Accepted 15 June 2008

Keywords:
Coronal mass ejections
Magnetic clouds
Interplanetary CMEs
Geomagnetic storms
Solar sources
Geoeffectiveness

ABSTRACT

Coronal mass ejections (CMEs) and high-speed solar wind streams (HSS) are two solar phenomena that produce large-scale structures in the interplanetary (IP) medium. CMEs evolve into interplanetary CMEs (ICMEs) and the HSS result in corotating interaction regions (CIRs) when they interact with preceding slow solar wind. This paper summarizes the properties of these structures and describes their geoeffectiveness. The primary focus is on the intense storms of solar cycle 23 because this is the first solar cycle during which simultaneous, extensive, and uniform data on solar, IP, and geospace phenomena exist. After presenting illustrative examples of coronal holes and CMEs, I discuss the internal structure of ICMEs, in particular the magnetic clouds (MCs). I then discuss how the magnetic field and speed correlate in the sheath and cloud portions of ICMEs. CME speed measured near the Sun also has significant correlations with the speed and magnetic field strengths measured at 1 AU. The dependence of storm intensity on MC, sheath, and CME properties is discussed pointing to the close connection between solar and IP phenomena. I compare the delay time between MC arrival at 1 AU and the peak time of storms for the cloud and sheath portions and show that the internal structure of MCs leads to the variations in the observed delay times. Finally, we examine the variation of solar-source latitudes of IP structures as a function of the solar cycle and find that they have to be very close to the disk center.

Published by Elsevier Ltd.

1. Introduction

Coronal mass ejections (CMEs) and corotating interaction regions (CIRs) are the two large-scale interplanetary (IP) structures that cause geomagnetic storms under certain conditions. CME structures originate at the Sun in closed field regions, while CIRs are formed at a distance from the Sun where high-speed streams (HSS) from coronal holes press against the slower ones ahead. The ability of IP magnetic structures in causing geomagnetic storms is referred to as geoeffectiveness, measured using one of the several indices such as Ap, Kp, AE, and Dst. In this paper, we consider only the Dst index, which is a measure of the ring current in the magnetosphere. IP structures are said to be strongly, moderately, and weakly geoeffective if they produce storms with $\mathrm{Dst} \leqslant -100\,\mathrm{nT}$, $-50\,\mathrm{nT} \leqslant \mathrm{Dst} < -100\,\mathrm{nT}$, and $-30\,\mathrm{nT} \leqslant \mathrm{Dst} < -50\,\mathrm{nT}$, respectively (see Loewe and Prolss, 1997 for a detailed discussion and comparison among storm indices). In this article, we use geoeffectiveness in the narrow sense of the ability of an IP structure in enhancing the ring current (as measured by the Dst index).

While moderate and weak storms may be caused by both CIRs and interplanetary CMEs (ICMEs), the intense ($\mathrm{Dst} \leqslant -100\,\mathrm{nT}$) storms are mostly caused by the latter (see e.g., Gosling et al., 1990). Only about 10–15% of the intense storms are due to CIRs (Kataoka and Miyoshi, 2006; Zhang et al., 2007) and the corresponding Dst index is close to $-100\,\mathrm{nT}$. Therefore, storms caused by ICMEs are of particular importance because of the high storm intensity. On the other hand, the CIR and ICME storms

* Tel.: +1 301 286 5885; fax: +1 301 286 1433.
E-mail addresses: nat.gopalswamy@nasa.gov, gopals@ssedmail.gsfc.nasa.gov (N. Gopalswamy).

1364-6826/$ - see front matter Published by Elsevier Ltd.
doi:10.1016/j.jastp.2008.06.010

Please cite this article as: Gopalswamy, N., Solar connections of geoeffective magnetic structures. Journal of Atmospheric and Solar-Terrestrial Physics (2008), doi:10.1016/j.jastp.2008.06.010

have different implications for the acceleration of MeV electrons in the magnetosphere (see, e.g., Miyoshi and Kataoka, 2005; McPherron and Weygand, 2006). For a given input energy, the CIR storms seem to produce a higher overall energy output in the magnetosphere (see, e.g., Lu, 2006; Turner et al., 2006 and other articles in Tsurutani et al., 2006). The CIR storms are also more numerous even though the storm intensity is small. Borovsky and Denton (2006) have listed a set of 21 aspects in which storms produced by ICMEs and CIRs differ.

ICME is the general name given to various types of IP structures resulting from CMEs. Magnetic clouds (MCs) are a subset of ICMEs when they have enhanced magnetic field, smooth magnetic field rotation, and low plasma beta as defined by Burlaga et al. (1982). The smooth magnetic field rotation refers to the flux-rope structure of the magnetic field (consisting of an axial magnetic field component and an azimuthal component perpendicular to the flux-rope axis). ICMEs without flux-rope structures are referred to as ejecta or non-cloud ejecta. The term "complex ejecta" is used when multiple ejecta are jammed together (Burlaga et al., 2001). ICMEs driving shocks have a sheath region between the shock and the MC/ejecta. The sheath is the compressed heliospheric magnetoplasma accumulated as the CME erupts and propagates into the IP medium. In this paper, we shall use various subsets of ICMEs to illustrate the geoeffectiveness and solar connections.

While the connection between the ICMEs and geomagnetic storms is well understood (see e.g., Gonzalez et al., 2002), the solar connection of ICMEs is often neglected citing the difficulty in associating CMEs with ICMEs (Gonzalez et al., 2007). However, the combination of multi-wavelength images of the inner corona available during the current solar cycle and the developments in understanding the IP propagation of CMEs have greatly helped in identifying pairs of CMEs and ICMEs. Quantitative link between CMEs and ICMEs is becoming clear from the point of view of magnetic flux and topology (Qiu et al., 2007), and kinematics (Gopalswamy et al., 2000a; Vrsnak and Zic, 2007). In-situ observations of ICMEs identify substructures such as shock, sheath, and driving ejects or MC, which is not possible for white-light CMEs, mainly because the shock standoff distance is too small near the Sun and it is difficult to identify substructures of CMEs when they are Earth-directed. Therefore, statistical methods have to be employed in connecting CME and ICME substructures.

Of particular importance are the sheaths of MCs, which may contain southward field and hence can lead to complex storms (see e.g., Kamide et al., 1998). There is increasing interest in the geoeffectiveness of sheaths because (i) they occur rather frequently (Huttunen et al., 2005) with intensity levels similar to the cloud portion (Gopalswamy et al., 2008a), (ii) they are connected to the heliospheric magnetic field accumulated in the front of propagating CMEs (see e.g., Kaymaz and Siscoe, 2006), and (iii) they result in enhanced geospace effects such as stronger auroral activity, stronger magnetotail field stretching, and larger asymmetry in the inner magnetosphere field configuration (Pulkkinen et al., 2007). Accordingly, this paper includes extensive discussion on the geoeffectiveness of MC sheaths.

Section 2 describes coronal holes and CMEs and their connection to geomagnetic storms. In particular, halo CMEs are compared with CMEs associated with large geomagnetic storms and MCs. Sections 3 and 4 deal with the properties and geoeffectiveness of MCs and their sheath. Section 5 discusses where on the Sun do the geoeffective structures originate and how these source locations change during various phases of the solar cycle. Section 6 contains discussion and conclusions.

2. Solar sources of geoeffective structures

The quiet IP medium consists of the Parker spiral magnetic field. In the ecliptic plane, this field has radial and azimuthal components with no out-of the-ecliptic component [the *Z*-component in the Geocentric Solar Ecliptic (GSE) coordinate system]. The ability of IP structures in causing geomagnetic storms arises because they possess this component. This section describes how coronal holes and CMEs contribute to Bz. Since the horizontal component of Earth's magnetic field is currently north pointing, the Bz of the IP structure needs to be south pointing (i.e., $Bz < 0$ or BzS) in order that the IP field couples to the geomagnetic field via the reconnection process as originally suggested by Dungey (1961). Although we measure the geoeffectiveness by the Dst index, the reconnection process in the dayside magnetosphere is the starting point for the geomagnetic storms.

2.1. Coronal holes

Coronal holes are observed as dark regions in X-ray and EUV images because they are cooler and less dense compared to the neighboring quiet coronal layers (see e.g. Krieger et al., 1973). Recurring geomagnetic storms were known long before the discovery of coronal holes and were attributed to magnetically active or M-regions on the Sun (Chapman and Bartels, 1962). It was later realized that the M-regions are in fact regions of enhanced unipolar magnetic patches on the Sun, at the bottom of coronal holes. The HSS originating from such coronal holes are supposed to derive their energy from the enhanced magnetic field. The coronal-hole chromospheres also have a distinct signature: the microwave emission above 15 GHz is enhanced in coronal holes compared to the quiet regions (Kosugi et al., 1986; Gopalswamy et al., 1997) indicating a higher temperature in these layers (Gopalswamy et al., 1999a, b). The quiet chromosphere in microwaves has a brightness temperature of ~10,000 K, while the coronal-hole chromosphere has an excess brightness temperature of ~500–2000 K. The microwave enhancements are associated with chromospheric network junctions and often display flare-like time variability (Gopalswamy et al., 1999a), consistent with the energy transfer to the solar wind via reconnection between closed and open fields (Tu et al., 2005).

Please cite this article as: Gopalswamy, N., Solar connections of geoeffective magnetic structures. Journal of Atmospheric and Solar-Terrestrial Physics (2008), doi:10.1016/j.jastp.2008.06.010

The HSS itself does not cause the storm. When the HSS impacts the preceding slower wind, an interaction region is formed, which indeed is the geoeffective structure (provided it contains BzS). Typically, the speed of the CIR structure is intermediate between those of the HSS and the preceding slow wind. The origin of Bz in CIRs is attributed to the Alfven waves, which are fluctuations perpendicular to the IP magnetic field (Belcher and Davis, 1971; Burlaga and Lepping, 1977; Tsurutani et al., 1995). Isolated coronal holes in the equatorial region and equatorward extensions of high-latitude coronal holes produce well-defined interaction regions in the IP medium. When the coronal holes remain stable, they produce similar streams when they rotate back to face Earth, thus causing storms recurring at 27-day intervals. Coronal holes evolve and can often be complex, so the recurrence may not be exactly at 27-day intervals. Complex coronal holes such as the one in Fig. 1 can lead to complex HSS structure at Earth. In the 15-day interval shown in Fig. 1, the solar wind speed varies from the slow-wind value (350 km/s) to about 700 km/s with four prominent intervals of high speed before falling back to the slow-wind value. A quick look at the EUV coronal image reveals that the coronal hole is longitudinally extended and the darkness is not uniform. The darkest regions are generally associated with the fastest streams. HSS originating from polar coronal holes dominate during solar minimum conditions (see e.g., Schwenn, 2006, and references therein).

There have been several attempts to relate coronal and coronal-hole properties to the observed solar wind velocities at 1 AU: coronal-hole area (Nolte et al., 1976), flux expansion rate (Wang and Sheeley, 1990), and magnetic reconnection (Fisk et al., 1999). Recently, Fujiki et al. (2005) showed that these may not be independent parameters and that a combination of the expansion factor and the photospheric magnetic field in the coronal-hole photospheres is best correlated with the solar wind speed.

2.1.1. Illustrative examples

Fig. 2 shows the solar wind properties associated with the coronal hole in Fig. 1 over an extended period. In addition to the magnetic field (in GSM coordinates), density, flow speed, and the Dst index are also shown. Four intervals in which the Dst index dropped to the storm level (−50 nT) are marked as 1–4. There was only one intense storm (Dst∼−100 nT for storm 1) associated with a large BzS interval. The magnetic field plot shows a clear bump in Bt corresponding to each storm and an associated density increase. Storm 4 had a Bz magnitude similar to that of storm 1 but the BzS duration and the solar wind speed were smaller. Thus, a suitable combination of BzS and speed decides the level of the resulting geomagnetic storm.

Fig. 3 shows an isolated compact coronal hole, which produced an HSS responsible for the first major geomagnetic storm in cycle 23. In the X-ray image obtained by the Yohkoh satellite, the coronal hole is completely dark except for a tiny bright point near the northern edge. This bright point is also seen in the magnetogram and in the microwave image. Contrary to the X-ray image, the magnetogram and microwave image show extended bright regions within the coronal hole. The magnetogram indicates that the magnetic field in the coronal-hole photosphere is enhanced with respect to the quiet region. The microwave enhancement occurs at network junctions, above which HSS seem to emanate. The coronal hole crossed the central meridian on October 20 at 07 UT. The fast solar wind at 1 AU started at 15 UT on October 22 and

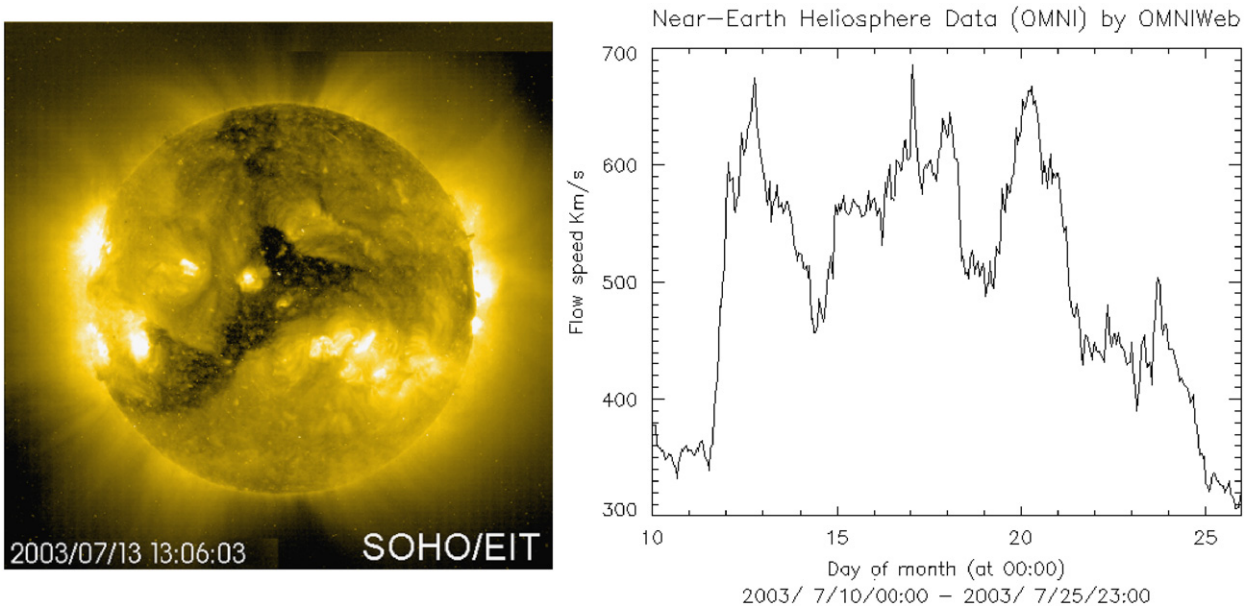

Fig. 1. Coronal hole (left) seen in a SOHO/EIT taken on July 13 2003 and the solar wind speed measured near Earth over a 15-day period in the coronal hole.

Please cite this article as: Gopalswamy, N., Solar connections of geoeffective magnetic structures. Journal of Atmospheric and Solar-Terrestrial Physics (2008), doi:10.1016/j.jastp.2008.06.010

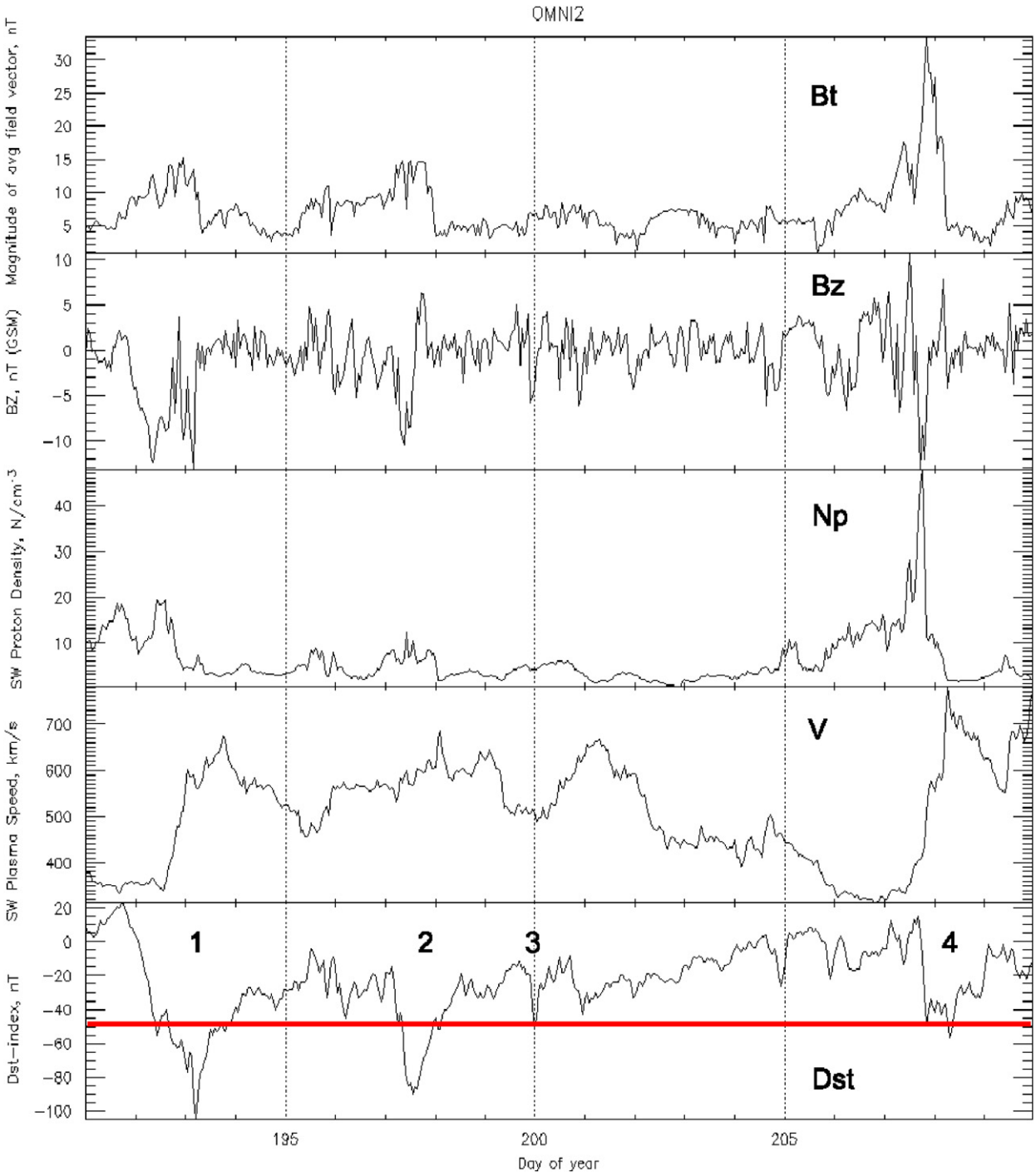

Fig. 2. Solar wind parameters (total magnetic field Bt, vertical component Bz, proton density Np, solar wind speed V) and the Dst index for a 19-day period in 2003. For four intervals (marked 1–4), the Dst index reached storm level (<-50 nT).

reached a peak speed of ~650 km/s at 07:30 UT on October 23 as observed by the Wind spacecraft (see Fig. 4). The magnetic field and density in the interaction region are enhanced by a factor of 3 with respect to the quiet solar wind values. During the 7-h interval bracketed by the two vertical lines, Bt and Bz are ~14 and ~−12 nT, respectively. Bz is negative throughout this interval, although with a lot of fluctuations. This interval is slightly shifted to the right from the density peak, but occurs well before the velocity peak. The main phase of the geomagnetic storm (see Fig. 4) started around 22 UT on October 22 and the Dst index reached the minimum value around 5 UT on October 23. The time elapsed from the central meridian passage of the coronal hole to the peak of the

Please cite this article as: Gopalswamy, N., Solar connections of geoeffective magnetic structures. Journal of Atmospheric and Solar-Terrestrial Physics (2008), doi:10.1016/j.jastp.2008.06.010

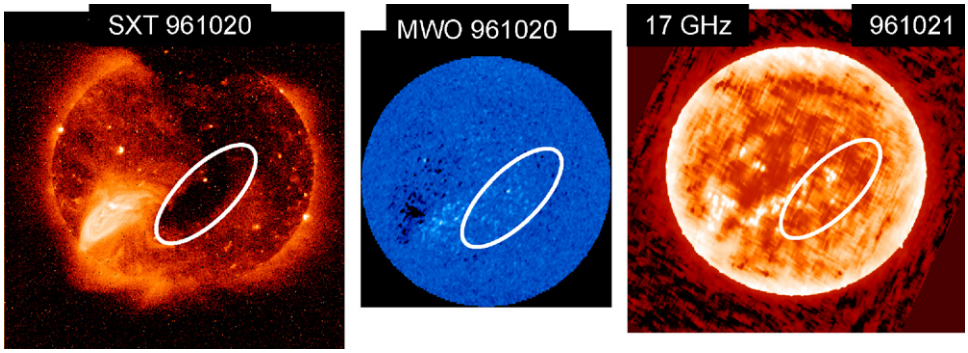

Fig. 3. (left) An isolated coronal hole from 1996 October 20-21 imaged by Yohkoh satellite's soft X-ray Telescope (SXT), (middle) Mount Wilson Observatory (MWO) magnetogram (white—positive and black—negative magnetic polarity), (right) Microwave image at 17 GHz from the Nobeyama Radioheliograph. The ellipse outlines the coronal hole as observed in X-rays.

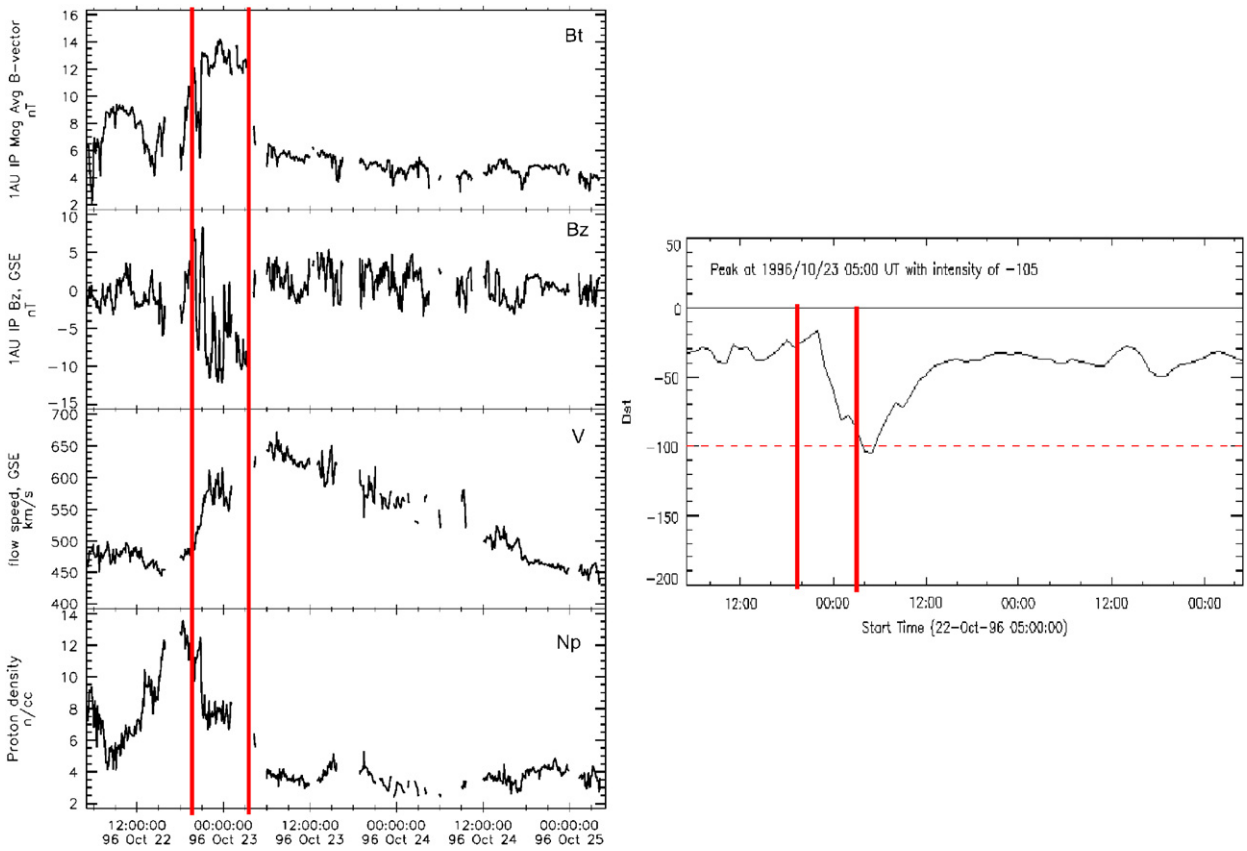

Fig. 4. (left) Total (Bt) and the vertical component (Bz) of the magnetic field, flow speed (V) and proton density (Np) in GSE coordinates. (right) Dst index from WDC. The vertical lines indicate the interval of negative Bz.

geomagnetic storm is 70 h, close to the statistical value (3.2 days) obtained by Vrsnak et al. (2007a, b). Note that the Dst index of this storm barely goes below −100 nT. The intensity level of major storms due to CIRs is generally around −100 nT. In cycle 23, there were a dozen such storms with Dst index ranging between −100 and −137 nT, with an average value of −115.4 nT. For comparison, the maximum intensity of ICME storms reached close to −500 nT (Gopalswamy et al., 2005a; Zhang et al., 2007).

2.2. Coronal mass ejections

CMEs were discovered roughly at the same time as coronal holes, first detected in the coronagraph images obtained on 1971 December 14 by NASA's OSO-7 spacecraft (Tousey, 1973). CMEs are large-scale magnetized plasma structures originating from active regions, filament regions, and active region complexes. The measured sky-plane speed of CMEs ranges from a few km/s to >3000 km/s (see e.g., Gopalswamy, 2004, 2006c; Yashiro

et al., 2004), with an average value of ~480 km/s, which is only slightly higher than that of the slow solar wind. CMEs have been observed by many space missions and the ground-based Mauna Loa K-coronameter. The Solar and Heliospheric Observatory (SOHO) mission's Large Angle and Spectrometric Coronagraph (Brueckner et al., 1995) has observed by far the largest number of CMEs over the longest time (more than a solar cycle), so we have complete knowledge on the range of CME properties.

2.2.1. CME substructures

CMEs are multi-thermal magnetized plasmas consisting of several substructures. From observations of CMEs originating from the limb, it has been inferred that slow CMEs have a three-part structure: bright frontal structure (farthest from the Sun), a dark void, and a bright prominence core (see Gopalswamy, 2004, and references therein). Prominence eruptions are readily observed from ground. The cavity has been identified as the earliest form of the flux rope observed as MC in the IP space. For CMEs occurring on the disk, it is difficult to see the substructures because of the occulting disk employed by coronagraphs obscures them. The three-part structure is often seen in eclipse pictures, which confirm that CMEs are formed out of pre-existing closed structures. For fast CMEs (those faster than the coronal fast mode speed), one expects a leading shock surrounding the whole CME.

Many authors have suggested that the flux-rope structure in CMEs is a fundamental physical structure that is a natural part of the eruption process (Marubashi, 1997; Owens et al., 2005; Gopalswamy, 2006a; Riley et al., 2006). For example, the ubiquitous post-eruption arcades seen in X-rays and EUV are primary indicators that flux ropes have erupted. There is an ongoing debate as to whether the flux ropes are formed during eruption due to reconnection, or the flux ropes exist before eruption, which are then expelled from the Sun during eruption. Another ubiquitous feature in closed field regions on the Sun is filaments, which are cool material suspended in the corona. Some people think the filaments are the flux ropes. It is true that the filaments are one of the fundamental structures of CMEs, but they occupy a small volume in the inner core of the CMEs. Others think the cavity is the flux rope, which means it is pre-existing (or formed by slow reconnection much before the main eruption). Making progress on these issues is very important because we can remote sense the magnetic field structure days before they arrive at Earth and cause geomagnetic storms.

From in-situ observations in the solar wind one can identify substructures such as the shock, sheath, and driving ejecta. It has been suggested that the white-light frontal structure of CMEs may be the solar counterparts of sheath ahead of ICMEs (Gopalswamy, 2003) and the outermost edge of the fast and wide CMEs is likely to be the shock (Sheeley et al., 2000). While the shocks are readily recognized in the in-situ data, it is difficult to detect them in white light, because the shock thickness is extremely small (much smaller than the currently available spatial resolution of coronagraphs). Type II radio bursts are the best indicators of shocks near the Sun (see Gopalswamy, 2006b for a review). Recently, spectroscopic observations have also been used to infer shocks near the Sun (see, e.g., Ciaravella et al., 2006). The sheath located between the shock and the flux rope is an entity that has information about both eruptive structures from the Sun and the heliospheric magnetic field. Sheaths observed at 1-AU are highly evolved compared to their near-Sun counterparts because of the continued accumulation of heliospheric material during the IP propagation of CMEs (see e.g. Kaymaz and Siscoe, 2006).

CMEs resulting in significant consequences in the heliosphere (e.g. geoeffective CMEs) generally start out with speeds >1000 km/s, which is higher than the fastest HSS observed. The apparent angular width of CMEs ranges from a few degrees to $>120^\circ$. CMEs wider than 60° are important for producing heliospheric impact. Sometimes CMEs appear to surround the Sun in the sky plane, known as halo CMEs (Howard et al., 1982). This is purely a geometrical effect, so the halo CMEs are no different from other CMEs. When halo CMEs appear on the Earthward face of the Sun, they head towards Earth and affect the magnetosphere causing magnetic storms, provided some substructure of the CME contains southward component of the magnetic field.

2.2.2. Illustrative examples

Fig. 5 shows a set of four CMEs originating from active region NOAA 0486, which was one of the largest regions during solar cycle 23 (Gopalswamy et al., 2005b). The first two CMEs originated very close to the center of the solar disk (the heliographic coordinates of the active region at the time of the eruptions were S15E15 and S19W05). Halos appearing symmetric about the solar disk generally originate close to the disk center. CMEs originating away from the disk center can also appear as halos, but are generally asymmetric with respect to the disk center. For example, the last two CMEs in Fig. 5 originated from western longitudes (W59 and W88), so they are asymmetric and heading westward. It is easy to see that symmetric halos make a direct impact on the magnetosphere, while only the eastern flanks of the asymmetric western CMEs do so. If the CMEs originate in the eastern hemisphere, their western flanks are likely to impact Earth.

The time variation of the Dst index following the four CMEs is also shown in Fig. 5. The halo CMEs on 2003 October 28 and 29 produced very intense geomagnetic storms (-363 and -401 nT, respectively). The CMEs on November 2 and 4 produced only a glancing impact to Earth's magnetosphere: a moderate storm (-84 nT) due to the November 2 CME and just a positive excursion of the Dst index known as sudden storm commencement due to the November 4 CME. Note that the Dst values used in Fig. 5 were "Provisional", which have changed slightly in the "Final" version available online at the World Data Center in Kyoto (http://swdcwww.kugi.kyoto-u.ac.jp/dstdir/index.html).

The center-to-limb variation of geoeffectiveness, illustrated in Fig. 5 for a single active region, has also been found to be true statistically (Gopalswamy et al., 2007). Fig. 6 shows the distribution of minimum Dst values

Please cite this article as: Gopalswamy, N., Solar connections of geoeffective magnetic structures. Journal of Atmospheric and Solar-Terrestrial Physics (2008), doi:10.1016/j.jastp.2008.06.010

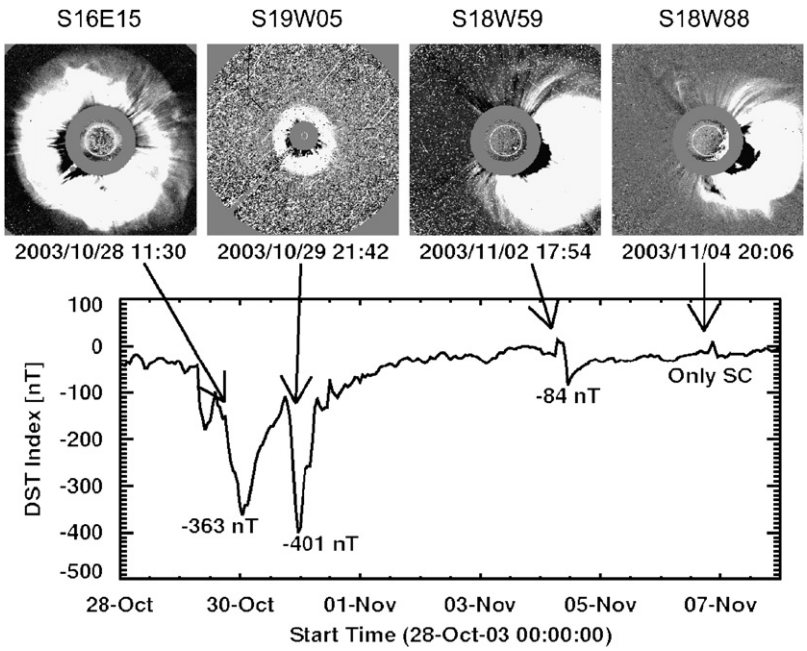

Fig. 5. (top) Four energetic CMEs during October–November 2003. The first two CMEs are halos, while the last two are not. The heliographic coordinates of the active region (NOAA 0486) from which the CMEs originated are indicated above each CME. The white circle represents the size of the optical Sun. The coronagraph images are superposed with EUV difference images showing activity close to the solar surface for all but the October 29 CME. (bottom) Plot of the Dst index for the period October 28 to November 8, 2003 where the large negative excursions represent geomagnetic storms (Dst values are noted). The Dst values (−363, −401, and −84 nT) were provisional values, which have been revised as −353, −383, and −69 nT, respectively. The positive excursions mark the arrival of the CME-driven shock at the magnetosphere (denoted by SC for sudden commencement of magnetic storm). (Adapted from Gopalswamy et al., 2005b).

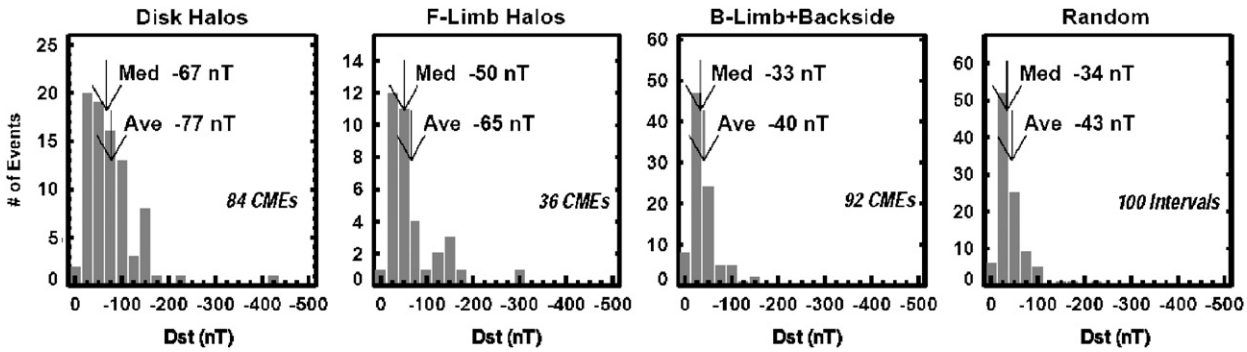

Fig. 6. Distribution of minimum Dst values following disk, frontside limb (F-Limb), backside limb (B-Limb), and completely backside halo CMEs. "Random" represents a control sample obtained by compiling minimum Dst values in 4-day intervals following the first day of every month in the study period (1996–2005). The average Dst value of the control sample is virtually the same as that in the B-limb+Backside halos (adapted from Gopalswamy et al., 2007).

following three different populations of halo CMEs: Disk, F-limb, and B-limb+Backside. The solar sources of disk halos have the central meridian distance (CMD)$\leqslant 45^\circ$ while those of F-limb halos have $45^\circ < \text{CMD} \leqslant 90^\circ$. B-limb halos have their sources slightly behind the limb. Backside halos move in the anti-Earthward direction from the backside of the Sun. A control sample of 100 Dst values was obtained as the minimum Dst values in a 4-day interval following the first day of each month in the study period. The control sample indicates the chance coincidence between a halo CME and a geomagnetic storm. For example, a geomagnetic storm may have been caused by a HSS or a non-halo CME but is attributed to a backside halo due to time coincidence. From Fig. 5 we see that the disk halos are followed by an average Dst of −77 nT and the F-limb halos by −65 nT. The B-limb and backside halos are not geoeffective because the Dst distribution following them (average = −40 nT) is similar to that (average = −43 nT) of the random sample.

Even though the overall association between CMEs and geomagnetic storms is straightforward in Fig. 5, the details are very different. For example, the storm on

Please cite this article as: Gopalswamy, N., Solar connections of geoeffective magnetic structures. Journal of Atmospheric and Solar-Terrestrial Physics (2008), doi:10.1016/j.jastp.2008.06.010

October 30 has a preceding minimum Dst value (−151 nT), while the October 31 storm has a clear single minimum even though both CMEs are full halos from the same active region. The difference between the two storms can be understood if we look at the solar wind structures that followed the two CMEs (see Fig. 7).

First, we note that Bz has different profiles for the two MCs: it starts out as north pointing and then changes to south pointing during the first MC, while remaining north pointing all the time in the second MC. The sheaths preceding both MCs have a large BzS, producing intense storms (−151 and −383 nT, respectively). The trailing portion of the first MC has a large BzS producing a huge storm, while the second MC has no BzS, hence the lack of storm. Thus, seemingly identical CMEs in white light can have completely different internal magnetic structure resulting in different magnetic storm profiles. As far as the CMEs are concerned, both are highly geoeffective (because of MC sheaths); from the point of view of MCs, the second one is not geoeffective at all.

2.2.3. Halo CMEs, geoeffective CMEs, and MC-associated CMEs

The above discussion centered on halo CMEs, which are an important population for geoeffectiveness. In fact, about two-thirds of halo CMEs originating on the Earthward face of the Sun have been found to be geoeffective (Zhao and Webb, 2003; Gopalswamy et al., 2007). This is a direct consequence of the fact that halo CMEs are more energetic than the average CMEs (Gopalswamy et al., 2007) and that halo CMEs typically originate close to the disk center. There is some disagreement on the geoeffectiveness rate of halo CMEs, mainly due to the ways in which halo CMEs and geoeffectiveness are defined (see e.g., Yemolaev and Yermolaev, 2006; Gopalswamy et al., 2007 and references therein). The property that halo CMEs

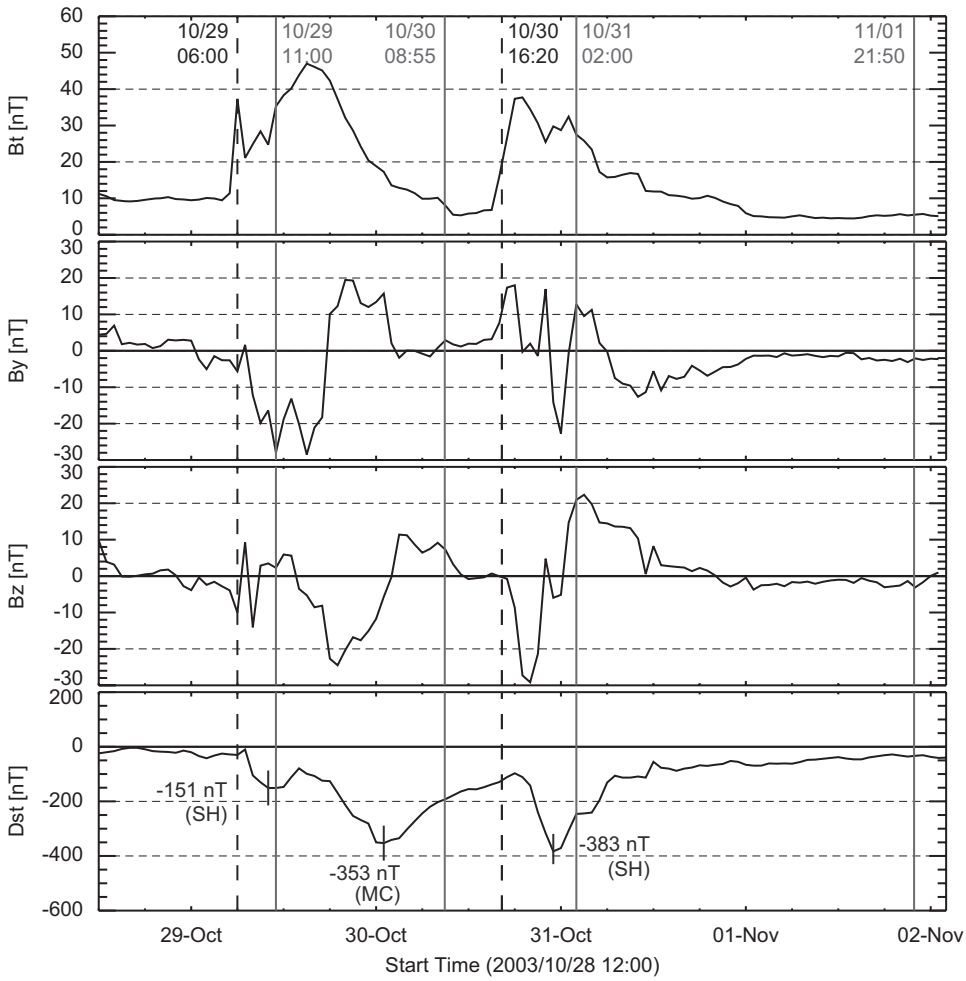

Fig. 7. Total magnetic field strength (Bt), By and Bz components from the Advanced Composition Explorer (ACE) available online at the OMNIWEB (http://omniweb.gsfc.nasa.gov) for the interval October 28 to November 2, 2003. The Dst index from the Kyoto World Data Center (http://swdcwww.kugi.kyoto-u.ac.jp/dstdir/) is shown at the bottom. The minimum Dst values are slightly different from the ones in Fig. 5 because these are final values. Vertical dashed lines mark shocks, while pairs of solid lines mark the ICME (MC) boundaries. The minimum Dst values in the sheath (SH) and cloud (MC) portions are also marked. The ICME boundaries were obtained from Malandraki et al. (2005).

Please cite this article as: Gopalswamy, N., Solar connections of geoeffective magnetic structures. Journal of Atmospheric and Solar-Terrestrial Physics (2008), doi:10.1016/j.jastp.2008.06.010

originate close to the disk center is also shared by CMEs associated with MCs. In fact, the majority of MCs observed in the IP medium are associated with halo CMEs (~63% if only full halos are considered and ~86% when width ⩾120° CMEs included—see Gopalswamy et al., 2000a, 2008a). Being a halo enhances the chances of a CME detected as an MC and affecting the magnetosphere head-on. It must be pointed out that non-halo CMEs can also cause geomagnetic storms so long as they impinge on the magnetosphere and contain BzS.

Fig. 8 compares the speeds of halo CMEs, MC-related CMEs, and strongly geoeffective CMEs (i.e., CMEs followed by a Dst index at or below −100 nT). The halo CMEs are presented in two groups (all and front-sided). Also shown is the speed distribution of MCs measured at 1 AU. The average speed of halo CMEs is larger by a factor >2 compared to the average speed of the general population of CMEs. The average speed of geoeffective CMEs is very similar to that of the halo CMEs, because most of the geoeffective CMEs are in fact halos. Some halos are not geoeffective and some geoeffective CMEs are not halos.

The average speed of MCs (measured at 1 AU) is considerably smaller than that of the corresponding white-light counterparts near the Sun. The MC speed distribution is the narrowest with an average speed (524 km/s) only slightly higher than that of the slow solar wind. The distribution of the corresponding white-light CMEs is much wider with an average speed of 774 km/s. Fast CMEs decelerate and the slow ones accelerate due to the strong coupling between CMEs and the solar wind resulting in a narrower distribution at 1 AU (Lindsay et al., 1999; Gopalswamy et al., 2000a, 2001). This is illustrated in Fig. 9 using a scatter plot between the CME speed near the Sun and the ICME speed measured in situ. MCs and non-cloud ICMEs are distinguished by different symbols.

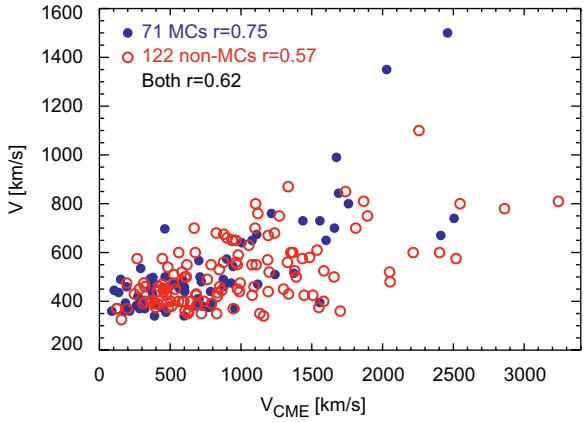

Fig. 9. Scatter plot of speeds for 203 CME–ICME pairs. MCs (open circles) and non-cloud ICMEs (closed circles) are distinguished. The correlation coefficient (r) is given on the plot for MCs, non-cloud ICMEs, and the combined set.

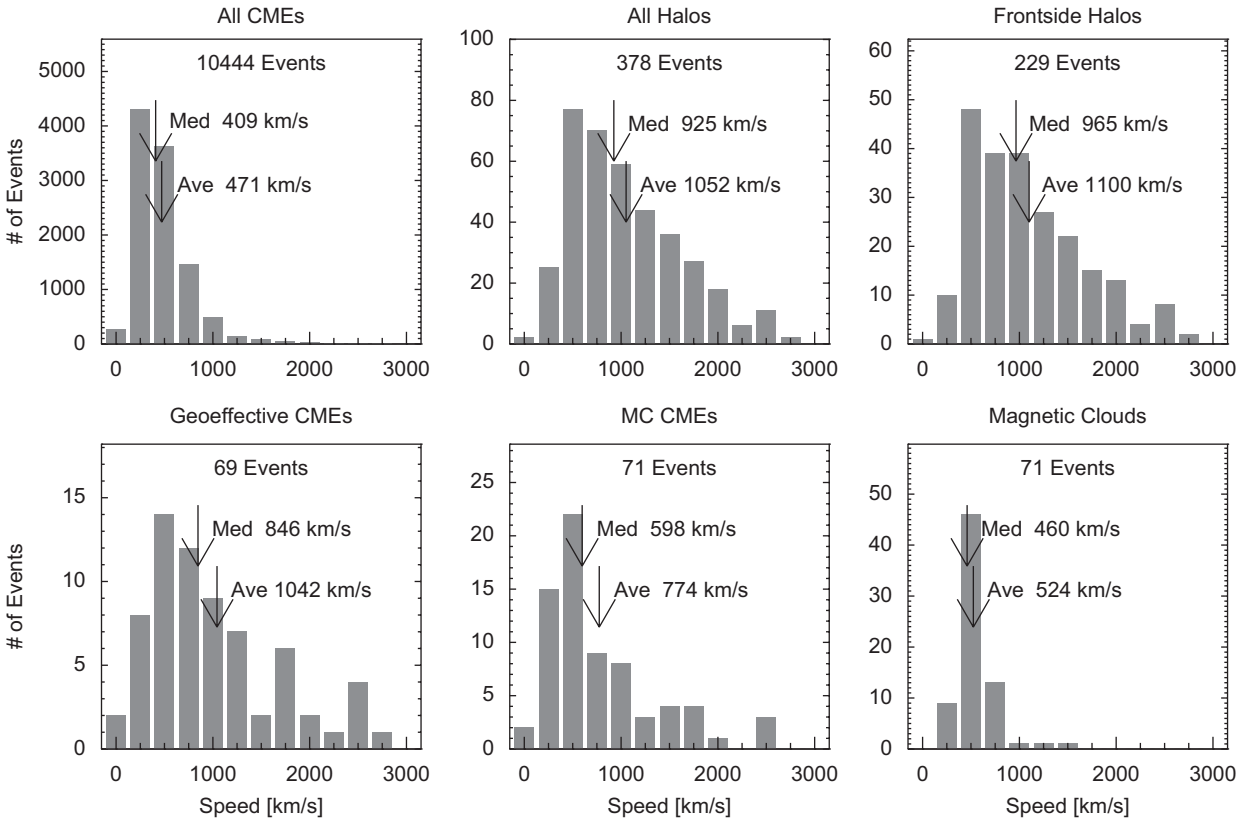

Fig. 8. Speed distributions of all CMEs, all halo CMEs, frontside halos, geoeffective CMEs, and MC-related CMEs, compared with that of MCs. Only those MCs with corresponding white-light CMEs are included in the last panel.

Please cite this article as: Gopalswamy, N., Solar connections of geoeffective magnetic structures. Journal of Atmospheric and Solar-Terrestrial Physics (2008), doi:10.1016/j.jastp.2008.06.010

The non-cloud ICMEs considered here were ejecta following shocks that did not have flux-rope structure. It is generally difficult to identify the boundaries of ICMEs that do not drive a shock, so it is difficult develop an exhaustive list of non-shock ICMEs. However, we do expect the non-shock ICMEs to be slow occupying the bottom left corner of the scatter plot in Fig. 9 and hence do not affect the conclusions from Fig. 9. While the CME speed ranges from ~100 km/s to >3000 km/s, the ICME speed ranges from >300 km/s to 1500 km/s. The correlation between CME and ICME speeds is the highest for MCs ($r = 0.75$) and lowest for non-cloud ICMEs ($r = 0.57$), while the combined set has an intermediate value ($r = 0.62$). Despite the large scatter, the ICME speed has a parabolic relationship with the CME speed as was demonstrated by Gopalswamy (2002). This is a direct consequence of the IP acceleration of CMEs (Gopalswamy et al., 2000a).

The fact that the average speed of MC-associated CMEs is the smallest (774 km/s) in Fig. 8 is worth noting. Although it is smaller than the average speed of all halos, it is close to the average speed (933 km/s) of disk halos (CMD$\leqslant$45°) reported by Gopalswamy et al. (2007). The average speed of limb halos (CMD>45°) is 1500 km/s. Thus, the smallest average speed of MC-related CMEs can be attributed to the projection effects because their solar sources are closest to the disk center. The slightly higher average speed of disk halos can be attributed to the wider source longitudes of disk halos (CMD$\leqslant$45°) compared to the narrower longitude distribution of MC-related CMEs. To illustrate this, we have compared the latitude and longitude distributions of CMEs with MCs and non-cloud ICMEs in Fig. 10. The non-cloud ICMEs used in Fig. 10 are the same as in Fig. 9. The latitude distributions are very similar and bimodal, suggesting that CMEs, which propagate to 1 AU typically originate in the active region belt (within 30° latitude). On the other hand, the longitudinal distributions are quite different. The MC-related CMEs originate close to the disk center (well within 30° longitude), while the longitude distribution of CMEs associated with non-cloud ICMEs is much wider and extend well beyond 30°. In fact, the longitude distribution of frontside halos reported by Gopalswamy et al. (2007) is quite similar to that of non-cloud ICMEs in Fig. 10.

3. Structure of ICMEs

One of the characteristic structures of shock-driving ICMEs is the sheath structure between the IP shock and the ejecta/MC readily recognized in in-situ observations (see Fig. 7). The sheath is well defined only when the ejecta or MC behind the shock is well observed. When the solar source of the IP structure is not close to the central meridian, the full extent of the sheath may not be observed because the observing spacecraft passes through a flank of the ICME. As we showed in Fig. 10, the solar sources of MCs are close to the central meridian, which

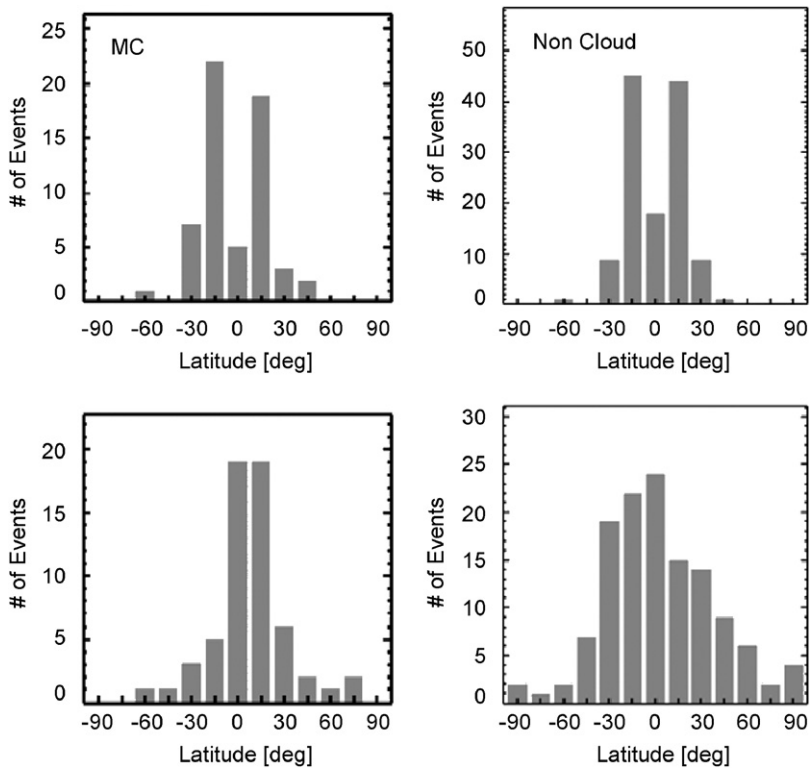

Fig. 10. Solar-source latitude and longitude distributions of MCs (left) and non-cloud ICMEs (right) observed during cycle 23. The latitude distributions are similar. The longitude distribution of non-cloud ICMEs is much wider than that of MCs.

Please cite this article as: Gopalswamy, N., Solar connections of geoeffective magnetic structures. Journal of Atmospheric and Solar-Terrestrial Physics (2008), doi:10.1016/j.jastp.2008.06.010

guarantees that the observing spacecraft passes through the nose of the ICME, so sheaths are fully observed. The number of MCs observed during solar cycle 23 is relatively large (99), of which 68 were driving shocks. About a third of the MCs do not drive shocks because they are very slow. Simultaneous observations of the solar counterparts by the SOHO coronagraph has made it possible to understand the entire ICME structure for a large sample. In the following, our discussion on ICMEs will concentrate on the subset observed as MCs, which are expected to apply to non-cloud ICMEs with appropriate geometric considerations.

3.1. Statistical properties of MCs

The magnetic field strength, proton density, bulk speed, and proton temperature of the 99 MCs measured at 1 AU are shown in Fig. 11 (data from Gopalswamy et al., 2008a compiled from the Magnetic Field Investigation (Lepping et al., 1995) on board Wind). All but the magnetic field strength are averages over the MC interval; the magnetic field strength is the maximum value (Bt) during the MC interval, which ranges from a few nT to several tens of nT (see e.g., Gopalswamy, 2006a). The average of Bt in MCs (18 nT) is more than three times that (~5 nT) of

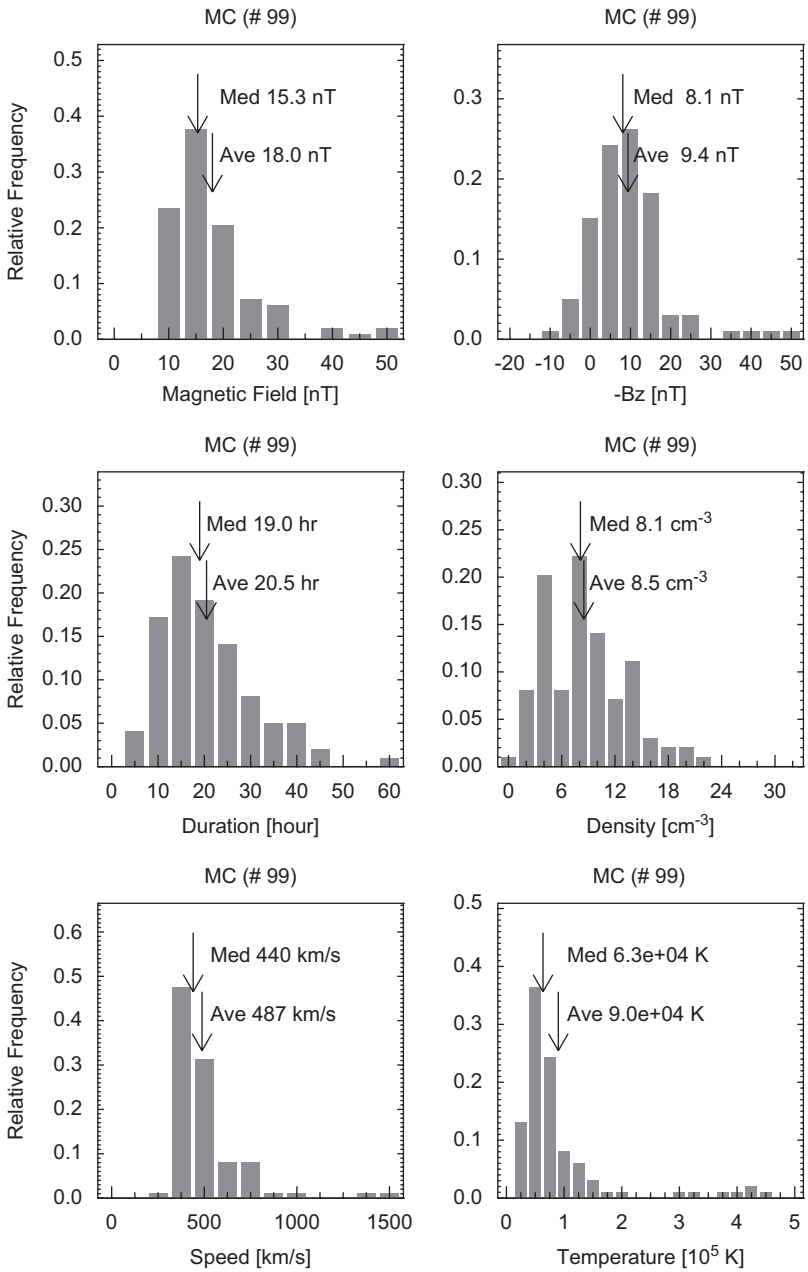

Fig. 11. Distributions of MC parameters: total magnetic field strength (Bt), strength of the *Z*-component (-Bz), duration, density, speed, and temperature. The average (Ave) and median (Med) values of the distributions are marked. For MCs with Bz > 0, the minimum value is used.

Please cite this article as: Gopalswamy, N., Solar connections of geoeffective magnetic structures. Journal of Atmospheric and Solar-Terrestrial Physics (2008), doi:10.1016/j.jastp.2008.06.010

the solar wind at 1 AU. The magnitude of Bz is also significantly higher with an average value of 9.4 nT. The duration of MCs ranges from a few hours to more than 40 h with an average value of 20.5 h. The average proton density in MCs ($\sim$8.5 cm^{-3}) is only slightly above the solar wind value. The mean speed of MCs (487 km/s) is also higher than that of the solar wind (440 km/s), but only by a small amount. The average proton temperature in MCs (9×10^4 K) is lower than that of the solar wind (1.1×10^5 K). The MC parameters described in Fig. 11 are consistent with those obtained from different samples (see, e.g., Lepping et al., 2006; Gopalswamy et al., 2000a; Huttunen et al., 2005; Echer et al., 2005). A complete set of properties of MCs detected by the Wind spacecraft can be found in Lepping et al. (2006).

When we consider shock-driving MCs, the average values are slightly different. The average MC speed is slightly higher (530 km/s), similar to the subset of MCs (shown in Fig. 8) associated with white-light CMEs. The average speed of sheaths is nearly the same (531 km/s), while the average of maximum speeds in sheaths is 567 km/s. The upstream solar wind speed averaged over a 6-h period preceding the shock is 417 km/s. These speeds are consistent with the average Alfvenic Mach number (2.9) of shocks detected at 1 AU (see Gopalswamy et al., 2005c). The shock-driving MCs also have a slightly higher average field in the cloud (Bt$\sim$19.4 nT and Bz$\sim$9.9 nT) with even higher values in the sheath (Bt$\sim$20.9 nT and Bz$\sim$10.9 nT). The temporal separation between the shock and MC arrivals averages to 12.1 h, very similar to the values obtained in the past studies (Gosling et al., 1987; Gopalswamy, 2006a).

It is also worth comparing the ICME properties with those of HSS at 1 AU. For simplicity, we consider subsets of ICMEs and HSS that resulted in intense geomagnetic storms during cycle 23. Fig. 12 compares the speed and magnetic field distributions of MCs, non-cloud ICMEs, and HSS. For CIRs, the maximum speed reached by the fast wind after the CIR interval is used. Bt and Bz are the maximum and minimum values, respectively in the CIR interval. For MCs, the speed, Bt and Bz correspond to the onset time of MCs at 1 AU. For non-cloud ICMEs, maximum values within the ejecta interval are used. The average speed of the fast wind is 616 km/s, compared 559 km/s for MCs and 636 km/s for non-cloud ICMEs. However, the average speed of the fast wind at the time of minimum Bz is only 453 km/s, which is less than the average MC speed. The average values of Bt and BzS are the highest in MCs. Even though the 1-AU values are similar, the speed evolution is completely different for ICMEs and CIRs. The HSS speed remains the same after reaching the maximum value in the near-Sun IP medium, while the CME speeds change due to the effective IP acceleration (which depends on the CME initial speed) and asymptotically approach the solar wind speed (see Fig. 9).

3.2. Internal structure of MCs

The magnetic structure of the MCs falls into four categories depending on how the southward component of the magnetic field changes direction from the front to back of the MC: south–north (SN), fully south (FS), north–south (NS), fully north (FN). SN and NS clouds have low inclination with respect to the ecliptic plane ($<45^\circ$), while the FN and FS clouds have higher inclination ($\geqslant 45^\circ$). Fig. 13 illustrates each of these MC types using Bt, Bz and Dst plots. Bz goes from negative to positive (south to north) values during the cloud interval for SN MCs, with the opposite variation for NS MCs. For the FS MCs, Bz is negative throughout the MC interval, while it is positive for the FN MCs. Since MCs have a flux-rope structure, each of these cloud types can be left handed or right handed as given by the Lundquist solution for the azimuthal field of MCs (see Burlaga, 1995 for details). If the handedness of the flux ropes is included, the SN clouds can be SEN or SWN depending on the direction of the Y-component of the MC magnetic field in GSE coordinates (E—east; W—west). FN and FS MCs show east–west rotation, so FS MCs can be ESW or WSE, while FN MCs can be ENW or WNE. The MC structure is important in establishing quantitative link to the source region on the Sun (see e.g., Bothmer and Schwenn, 1994; Mulligan et al., 1998). For the purpose of geoeffectiveness, the handedness is less important, so we confine our discussion to the four basic types, viz., SN, NS, FS, and FN. For simplicity, the SN and NS MCs are sometimes referred to as bipolar MCs because of the *Z*-component has both north- and south-pointing fields during the MC interval; the FN and FS MCs are referred to as unipolar because the *Z*-component points solely to the north or to the south during the MC interval. Thus, the southward component of the magnetic field has a well-defined time profile in MCs, depending on the MC type (unipolar or bipolar, see e.g., Zhang et al., 2004 and references therein).

Fig. 14 compares the distributions of Bt and average speed in the cloud and sheath portions of various MC types. The average kinematic properties of the cloud types are very similar to those of the combined set. The average and median Bt values in the cloud and sheath portions are generally similar and are elevated with respect to the ambient solar wind values by a factor of 3–4. The difference arises only in the Bz time profile, which is important for geoeffectiveness (to be discussed in Section 4).

3.3. Solar-cycle variation of MC types

Some interesting results are obtained when the solar-cycle variation of the MC types are considered separately. Fig. 15 shows the numbers of various MC types binned over the three phases of the solar cycle. The SN clouds were the largest in number (39%) during cycle 23, being two times the numbers in each of the other types (FS—19%), NS—21%, and FN—20%). The rising phase runs from 1996 to 1998 (inclusive). The maximum phase includes the years 1999, 2000, 2001, and part of 2002 (until May). In May 2002, the polarity reversal at the solar poles was completed and the global solar field acquired a new configuration (Gopalswamy et al., 2003). We take this epoch to be the end of the solar maximum phase. The declining phase starts from June 2002 to the next

Please cite this article as: Gopalswamy, N., Solar connections of geoeffective magnetic structures. Journal of Atmospheric and Solar-Terrestrial Physics (2008), doi:10.1016/j.jastp.2008.06.010

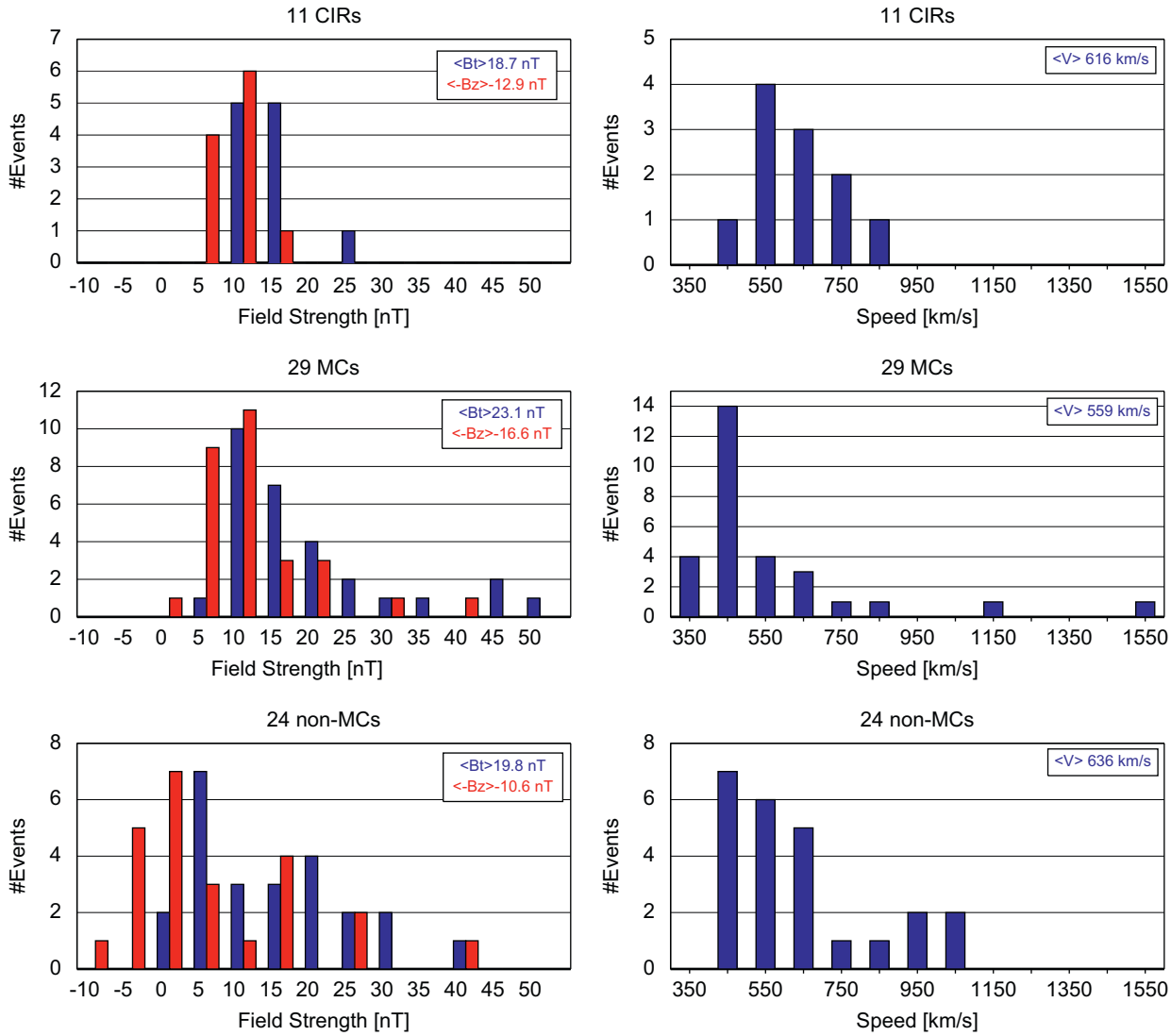

Fig. 12. Distributions of magnetic field strength (left) and speeds (right) measured at 1 AU for CIRs, MCs, and non-cloud ICMEs that caused intense geomagnetic storms (Dst < −100 nT). Bt and Bz correspond to the maximum values in the CIR or ICME intervals. For CIRs, the maximum speed reached by the solar wind is used (generally after the CIR). For MCs, the speed at the time of MC arrival is used. For non-cloud ICMEs, the maximum speed within the ICME interval is used. The average values of the distributions are given on the plots.

minimum, but we approximate it to the end of 2005. The three phases do not have the same length, but long enough so that sufficient number of each MC type can be found in each phase. The bipolar MC numbers in Fig. 15 vary with an opposing tendency as a function of time: the number of SN clouds declines from the rise phase to the declining phase, while the NS clouds increase in number through these phases. The numbers of FS and FN MCs remain roughly the same in the three phases. The predominance of SN MCs over the NS MCs is consistent with what is expected for odd cycles (Mulligan et al., 1998). The number of bipolar MCs (SN+NS) is relatively constant (23, 22, 15 during rise, maximum, and declining phases) as noted by others (Li and Luhmann, 2004; Huttunen et al., 2005; Echer et al., 2005), which probably arises from the opposite trends in the number of SN and NS clouds. The number of unipolar (FS+FN) MCs shows a slight decline (17, 12, 10) as a function of time.

The declining SN number and increasing NS number is consistent with the change in the direction of the global solar field which is thought to decide the leading field of MCs (Crooker, 2000). The global solar field was southward before the polarity reversal in May 2002 and then turned northward. However, we do not know if the leading fields of MCs are formed out of the global field. If MCs form due to reconnection in the source region, one expects the closed field lines overlying the filament (or polarity inversion line) to become the leading edge of the MC due to reconnection. Some quantitative evidence for such a relationship has been presented by Qiu et al. (2007): the reconnected flux as measured at the feet of the post-eruption arcades is very close to the poloidal flux of MCs

Please cite this article as: Gopalswamy, N., Solar connections of geoeffective magnetic structures. Journal of Atmospheric and Solar-Terrestrial Physics (2008), doi:10.1016/j.jastp.2008.06.010

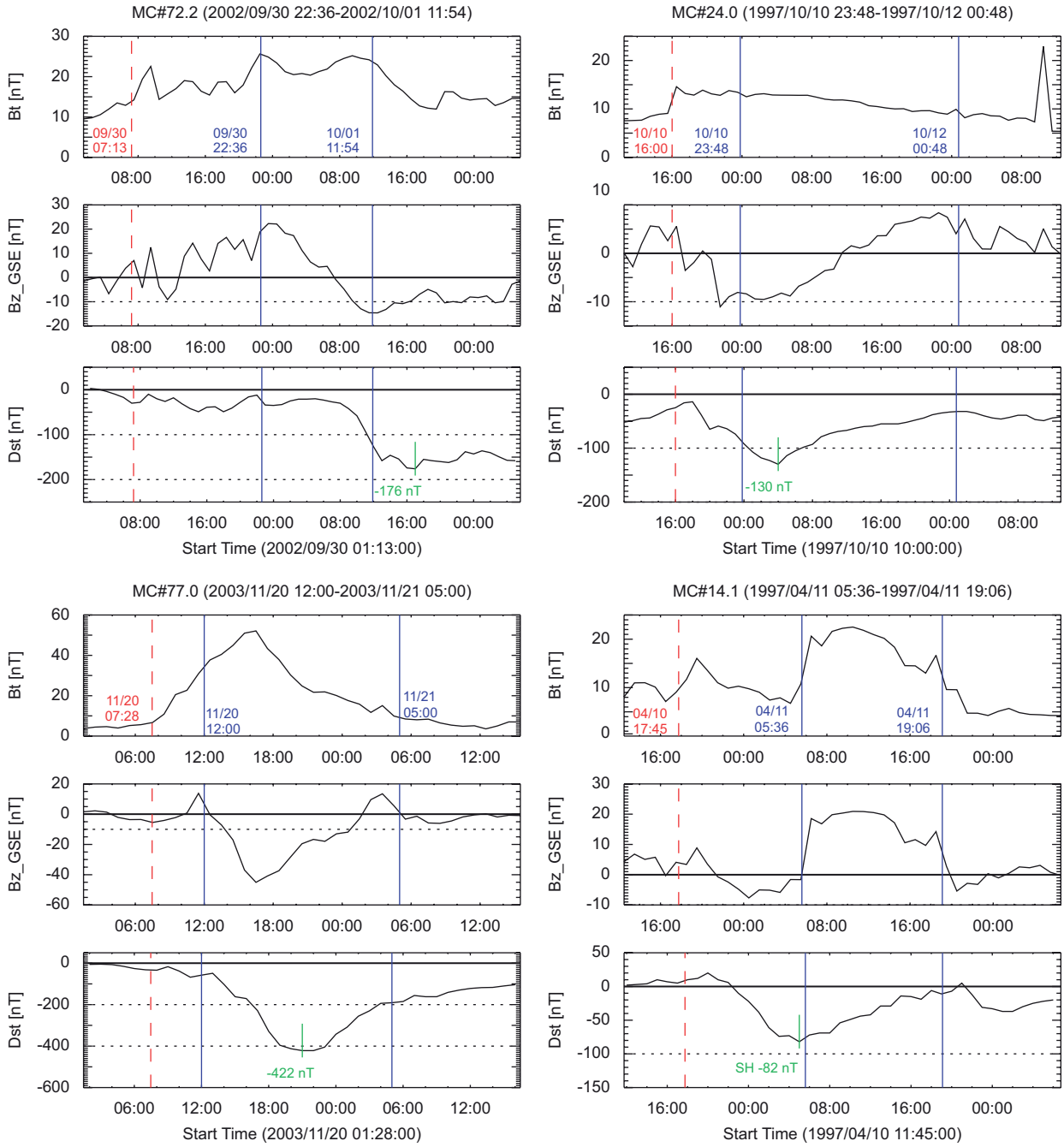

Fig. 13. Plots of Bt, Bz, and Dst as a function of time showing the four types of MCs. Top panel: bipolar MCs (NS on the left and SN on the right). Bottom panel: unipolar MCs (FS on the left and FN on the right). The interval between the solid vertical lines corresponds to MCs. The vertical dashed lines denote shocks ahead of MCs. Times of the MC boundaries and shocks are indicated on the plots. Minimum Dst values of the associated storms are noted. The geoeffectiveness of MCs (or any IP structure) crucially depends on the time and magnitude of BzS. For the FN MC, the storm is due to the BzS in the sheath (indicated by SH).

measured in situ. The MC sheath is the global heliospheric field overlying the eruption region. A proper understanding of the magnetic field structure near the Sun will greatly enhance our ability in predicting the geoeffectiveness of CMEs when they are still near the Sun. However, we are long way away in making direct measurements of the CME magnetic field in the corona.

3.4. Speeds and field strengths

The speed and the magnetic structure of ICMEs are important quantities which determine how ICMEs couple with the magnetosphere. Recall from Fig. 9 that the ICME speeds are related to the CME speeds via the IP acceleration (see also Lindsay et al., 1999; Gopalswamy et al.,

Please cite this article as: Gopalswamy, N., Solar connections of geoeffective magnetic structures. Journal of Atmospheric and Solar-Terrestrial Physics (2008), doi:10.1016/j.jastp.2008.06.010

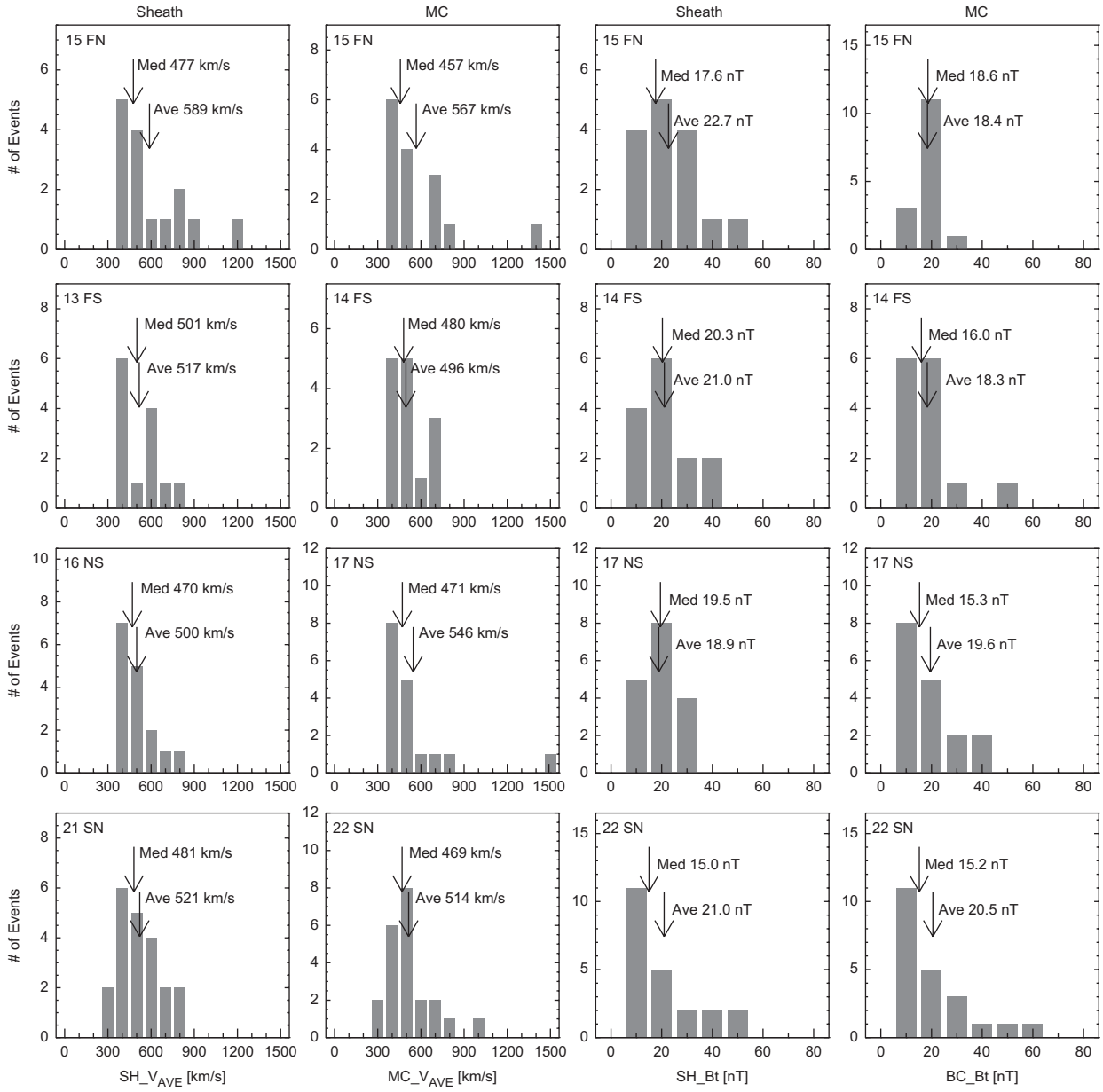

Fig. 14. Average speed (left) and maximum field strength (right) of sheaths and MCs for the four cloud types. The average and median values of the distributions are marked on the plots.

2000a, 2001). The azimuthal flux of MCs also seems to be related to the reconnected magnetic flux in the erupting active region (Qiu et al., 2007). Gonzalez et al. (1998) found a good correlation between the peak magnetic field and the peak speed in 30 MCs (correlation coefficient $r = 0.75$) (all correlations are anti-correlations). However, they did not find a good correlation between the speed and field strength for non-cloud ejecta, which they attributed to the geometrical effect preventing accurate measurement of field strength in the cloud. Echer et al. (2005) confirmed Gonzalez et al. (1998) results but the correlation coefficient was smaller ($r = 0.35$) for a set of 149 MCs. Gopalswamy et al. (2008a) reported an intermediate correlation ($r = 0.56$) for a set of 99 MCs in cycle23. Owens et al. (2005) found no correlation between speed and magnetic field in 30 MCs. However, they found a good correlation between the speed and magnetic field in sheaths. They suggested that the peak speed of MCs used by Gonzalez et al. (1998) might reflect the sheath speed, consistent with their observation. However, this suggestion does not apply to Gopalswamy et al. (2008a) who used average MC speeds.

Fig. 16 compares the speed-field strength correlations for MCs and sheaths. A subset of 68 shock-driving MCs

from Gopalswamy et al. (2008a) is used for this plot. The best correlation is obtained between V and Bt in sheaths. The correlation coefficient ($r = 0.77$) is in agreement with Owens et al. (2005) for sheaths. Even the sheath Bz is reasonably correlated with sheath V ($r = 0.55$). Interestingly, the near-Sun CME V also shows a positive correlation with the Bt and Bz in the sheath, with $r = 0.54$ and 0.32, respectively. These correlations are better than the corresponding ones in MCs ($r = 0.42$ for V–Bt and $r = 0.20$ for V–Bz). This is a significant result, given that the sheath and CME parameters are measured days apart and at different locations in the heliosphere (near the Sun for CMEs and at 1 AU for MC sheaths). The CME V–Bt scatter plots in Fig. 16 are similar to the CME V–Bt plot of Lindsay et al. (1999), who used ICME Bt (not separating MCs) made at a heliocentric distance of ~0.7 AU. The CME speed—Bz correlation in Fig. 16 is also weaker than that of Yurchyshyn et al. (2004), who used only 14 events and did not separate cloud and non-cloud ICMEs (their Bz values were the larger of the ICME and sheath values). Since CMEs accumulate the ambient heliospheric magnetic field into the sheaths, it is significant that the relationship is preserved over the Sun-Earth distance and consistent with the identification of the CME frontal structure with the ICME sheath observed in situ (Gopalswamy, 2003).

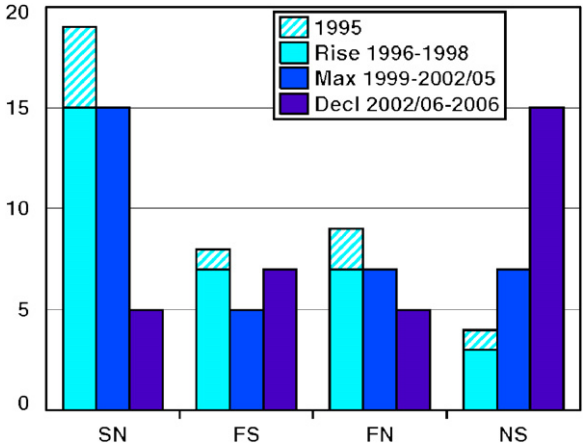

Fig. 15. Solar-cycle variation of the number of MCs in each cloud type, binned by phases of cycle 23: rising (1996–1998), maximum (1999–May 2002), and declining (June 2002–2005). The hashed portion corresponds to the year 1995, which belongs to cycle 22.

What does all this mean? The CME speed at the Sun is determined by the free energy available in the eruption region. MC field is likely to be related to the field ejected from the Sun with appropriate modification due to propagation effects. However, the distinct sheath and MC features observed in the IP medium are not distinguished by white-light observations, especially for the Earth-directed CMEs. The sheath is the compressed ambient material, the deepest layers of which may in fact be the outermost white-light features observed near the Sun. In faster CMEs, the compression enhances the field significantly resulting in the positive correlation.

4. Geoeffectiveness of MCs and sheaths

It is clear from Fig. 7 that bipolar MCs are highly likely to be geoeffective because they contain BzS either in the front or in the rear section. On the other hand, the unipolar MCs can be either geoeffective (FS type) or not geoeffective (FN type) depending on the polarity of the axial magnetic field (Yurchyshyn et al., 2001; Gopalswamy

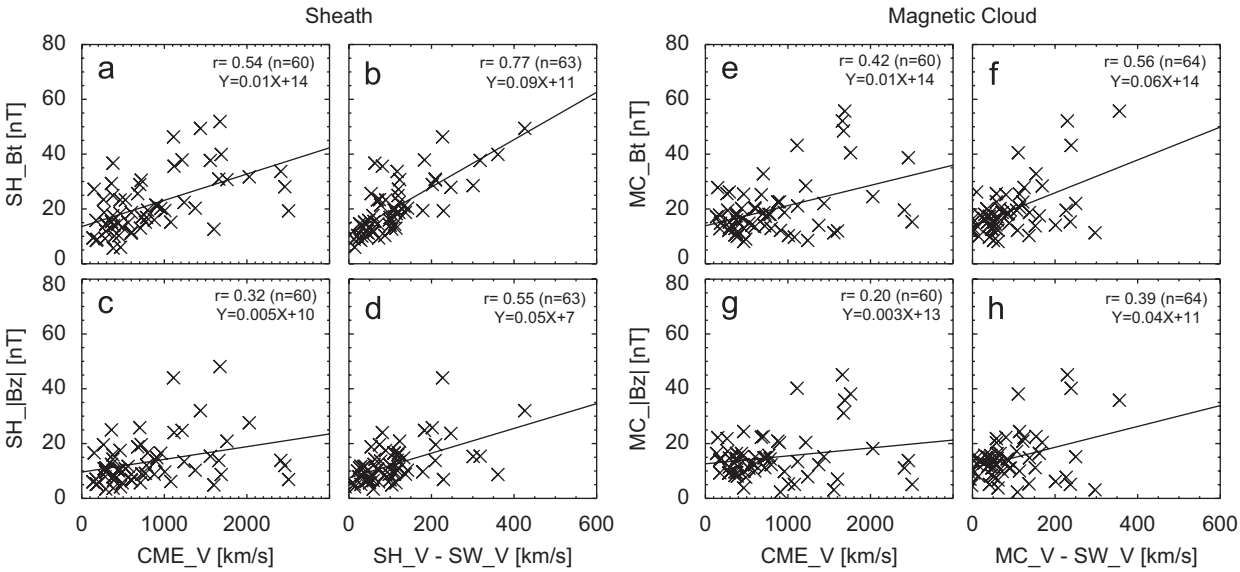

Fig. 16. Relation between speeds and magnetic field strengths in sheaths and MCs: (a) CME speed (CME_V vs. Bt in MC, (b) CME_V vs. |Bz|, (c) MC speed (MC_V) vs. Bt in MC, (d) MC_V vs. |Bz| in MC, (e) CME_V vs. Bt in sheath, (f) CME_V vs. |Bz| in sheath, (g) sheath speed (SH_V) vs. Bt in sheath, (h) SH_V vs. |Bz| in sheath. The correlation coefficient (r), the number of data points used in the correlation (n), and the equation of the regression line are given on each plot.

Please cite this article as: Gopalswamy, N., Solar connections of geoeffective magnetic structures. Journal of Atmospheric and Solar-Terrestrial Physics (2008), doi:10.1016/j.jastp.2008.06.010

et al., 2005a). Recall that the second MC in Fig. 7 was of FN type (fully northward), so it did not produce any storm. However, the sheath of this MC had Bz = −30 nT, which resulted in a superstorm (Dst∼−400 nT). In fact, 55% of the FN MCs had geoeffective sheaths, making them as important as other types of MCs for geoeffectiveness (Gopalswamy et al., 2008a). In addition to BzS, which is the primary requirement for producing geomagnetic storms, the CME speed and magnetic field also affect the intensity of the geomagnetic storms.

4.1. Storm intensity and MC properties

Various combinations of the speed and magnetic field strength of IP structures have been found to be correlated with the Dst index (Akasofu, 1981; Wu and Lepping, 2002; Yurchyshyn et al., 2004; Srivastava and Venkatakrishnan, 2004 and references therein). Here we consider a simple product of the speed of the IP structure with Bt and Bz in the structure. We also consider CME speeds, and use the Bt and Bz in the corresponding MCs and sheaths because we do not have direct measurement of magnetic fields in CMEs near the Sun. We do expect the CME speed to be related to the MC and sheath speeds as discussed in Section 3.4.

4.1.1. Storm intensity vs. speed and magnetic field

The top row in Fig. 17 compares the dependence of sheath and MC Dst on the corresponding speeds as well as on CME speeds. Note that a sheath–MC pair is associated with a single white-light CME. Both sheath and cloud Dst values have the smallest but positive correlation ($r = 0.49$ and 0.46, respectively) with CME V. Sheath and cloud Dst values have a significant correlation with their speeds ($r = 0.67$ and 0.65, respectively). The second row in Fig. 17 shows how sheath and cloud Dst values depend on their Bt and Bz. Dst in MCs is best correlated with Bt in the cloud portion ($r = 0.84$). All correlations are at are better than $r = 0.73$, making the magnetic field in the sheath and cloud portions an important factor contributing to the storm intensity.

4.1.2. Storm intensity vs. speed and magnetic field products

Dst has a better correlation with the speed—magnetic field products compared to the one with single parameters (speed or magnetic field). For example, the sheath Dst vs. SH_Bt × CME_V has $r = 0.72$ (Fig. 17e). The corresponding value for the cloud portion is $r = 0.80$ (Fig. 17m). If the CME_V is replaced by the sheath and cloud speeds, we get the higher correlations: $r = 0.78$ (sheaths, see Fig. 17f) and $r = 0.84$ (MCs, see Fig. 17n). When Bt is replaced by −Bz (see the bottom row of Fig. 17) we get the highest correlations ($r = 0.83$ to 0.90). The highest Dst correlation is obtained with the product of speed and Bz in MCs ($r = 0.90$), closely followed by the product of speed and Bz in sheaths ($r = 0.86$). Note that the Dst correlations with the products of CME speed with the MC fields or the sheath fields remain high. When measurements of CME magnetic fields become possible, this correlation can be directly confirmed and can be put to space weather applications. It must be pointed out that the number of points at high values of the X-coordinate in Fig. 17 is small, even though we have used data from almost the whole of a solar cycle because such occurrences are relatively rare.

4.2. MC types and the geoeffectiveness of sheath and cloud portions

Dividing MCs into the four types also has the advantage of knowing a priori when the storm likely peaks. Sheaths precede the MC arrival at Earth, so sheath storms usually precede the MC arrival. As for MCs, the delay time between MC arrival and storm peak (Dst minimum) depends on the MC type (which tells us where in the MC interval one would expect BzS). Some MCs have BzS both in the sheath and the cloud portions. When both sheath and cloud portions are geoeffective, double-dip storms occur (see e.g., Kamide et al., 1998), again depending on the internal structure of MCs.

4.2.1. Dst comparisons

Fig. 18 (left two columns) compares the Dst distributions in the sheath and cloud portions. The average values of Dst index associated with the cloud and sheath portions significantly exceed the geoeffectiveness level (Dst ⩽ −50 nT). The only exception is the FN MCs, which are not geoeffective. The negative Dst value for a single FN MC is due to noise and is shown for completeness. The average Dst index due to the sheaths of FN MCs are at the intense storm level (Dst ⩽ −100 nT). This does not happen for the sheaths of any other MC type. Such high storm level can be found in the cloud portion of FS MCs because of the BzS expected throughout MC interval. It is not clear why intense sheath storms should occur specifically for one type of MC. We recognize that 75% of the 20 FN MCs occurred during the rise and maximum phases of cycle 23 (see Fig. 15), when the global solar field is south pointing. Furthermore, FN MCs have high inclination with respect to the ecliptic plane, so draping occurs primarily parallel to the MC axis enhancing the likelihood of producing BzS in the sheath. Similar situation is expected for the sheaths of FS MCs, but the storm level is almost 50% lower. The relative orientation between MC and sheath fields may lead to different sheath compression. Further investigation is needed using data from other solar cycles to arrive at firm conclusions.

4.2.2. Delay-time comparisons

The Dst minimum generally occurs ∼2 h after the BzS reaches its peak value (Gonzalez and Echer, 2005). The time of Dst minimum can precede or follow the MC arrival at Earth depending on which substructure has BzS (i.e., is geoeffective). We define the time elapsed from the MC arrival at 1 AU to the time of Dst minimum as the delay time. The right two columns of Fig. 18 compare the delay times of the sheath and cloud storms. The sheath storms have a negative delay as expected (average = −3.2 h). The delay can be understood by referring to Fig. 7, which shows two examples of sheath storms. The first sheath

Please cite this article as: Gopalswamy, N., Solar connections of geoeffective magnetic structures. Journal of Atmospheric and Solar-Terrestrial Physics (2008), doi:10.1016/j.jastp.2008.06.010

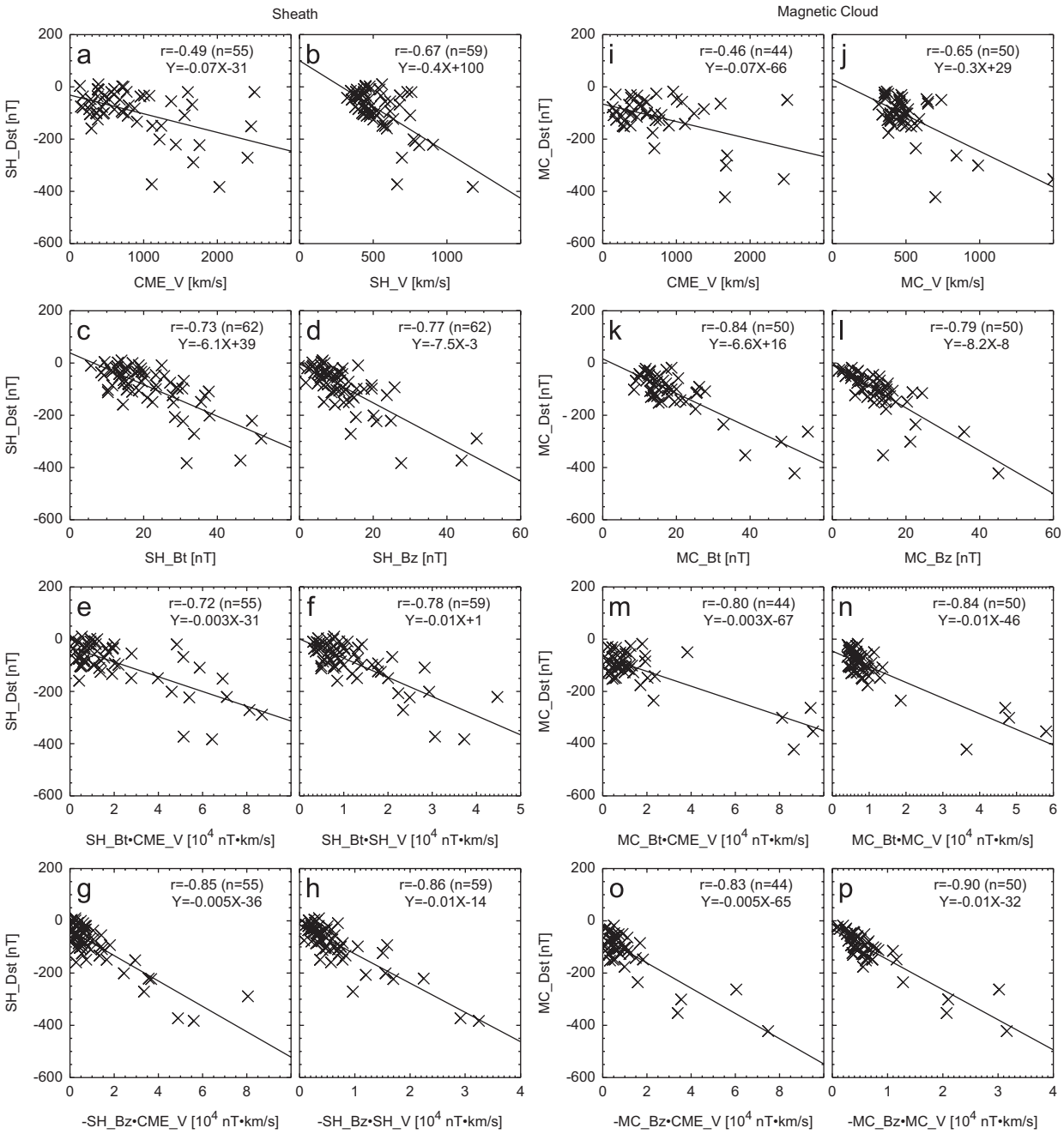

Fig. 17. Scatter plots of speeds, magnetic fields, and their products with Dst index in sheaths (left two columns) and MCs (right two columns: (a) sheath Dst (SH_Dst) vs. CME speed (CME_V), (b) SH_Dst vs. sheath speed (SH_V), (c) SH_Dst vs. sheath Bt (SH_Bt), (d) SH_Dst vs.-SH_Bz, (e) SH_Dst vs. SH_Bt*CME_V, (f) SH_Dst vs. SH_Bt*SH_V, (g) SH_Dst vs.-SH_Bz*CME_V, (h) SH_Dst vs.-SH_Bz*SH_V, (i)–(p) same as in (a)–(h) except the speed and field are in the cloud portion.

storm actually has a positive delay (+2 h) because the sheath is very short so the minimum Dst index occurs after the MC arrival. The second sheath storm has a clear negative delay (−3 h) because the duration of BzS in the sheath is extended. The only cloud storm in Fig. 7 has a large positive delay (17 h) because the MC is of NS type, so the geoeffective part is towards the end of the MC. The absolute value of the delay time of the sheath storms is the smallest (average = −1.6 h) for FN MCs and the longest for FS and NS types (average = −4.4 h). The sheath storms of SN MCs have an intermediate delay (average = −2.7 h). Among the cloud storms the smallest delay is for SN MCs (average = 5.5 h) and the largest is for NS clouds (average = 18.6 h). The FS clouds have an intermediate delay (average = 9.3 h). The onset of sheath storms is very close to the shock arrival time, while the

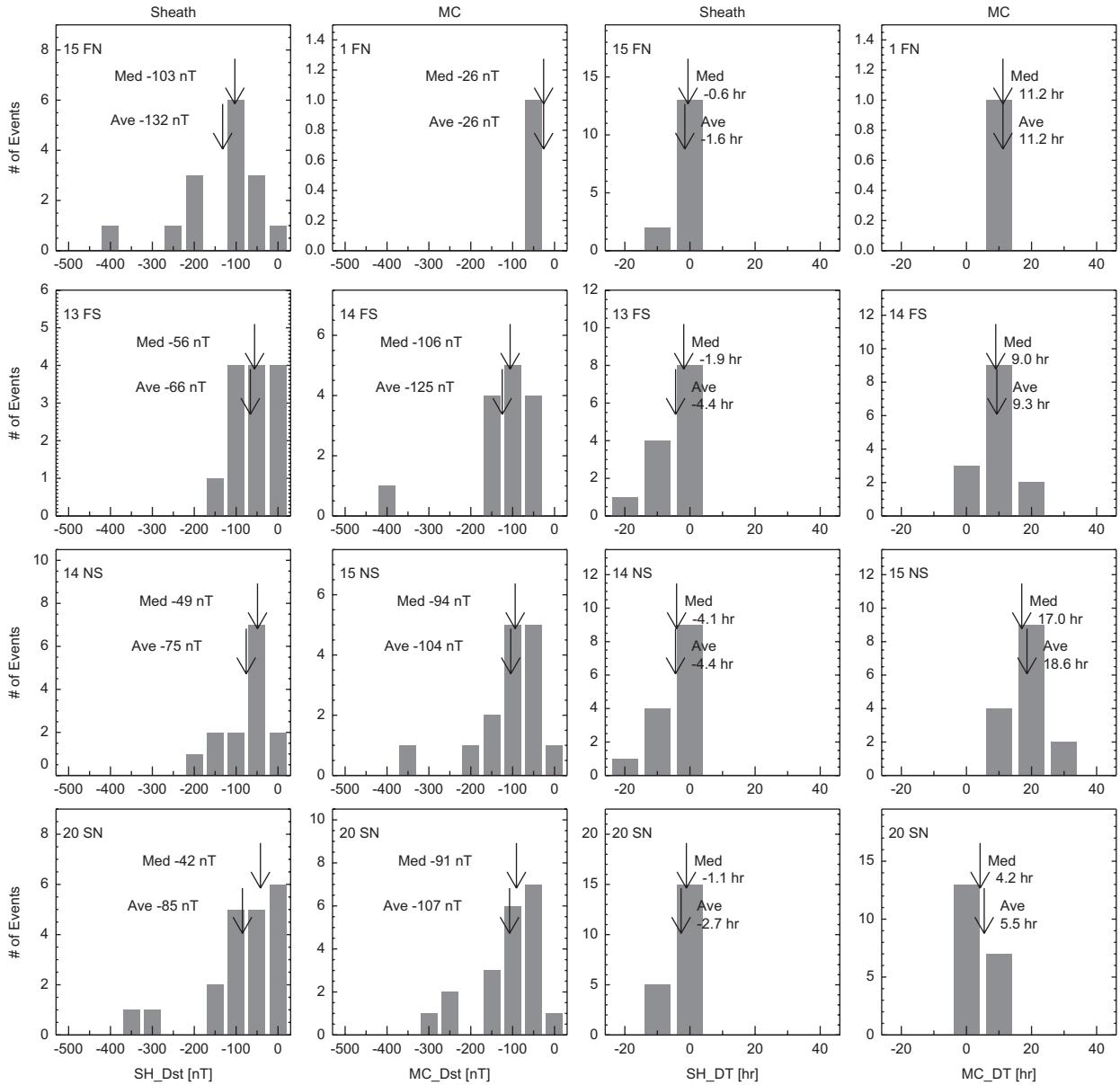

Fig. 18. (left) distributions of Dst index in the sheath and cloud portions for the four MC types. (right) Distributions of delay time of Dst minimum with respect to the MC arrival at Earth. The average (Ave) and median (Med) values of the distributions are indicated on the plots.

cloud storms can be delayed by as much as the Sun–Earth travel time of some fast-transit shocks. For example, the 2003 October 29 shock took 18.9 h to arrive at Earth, but the cloud storm peaked 19 h after the shock arrival. However, the sheath storm of this event occurred in ~4 h from the shock arrival. On the other hand, the 2003 October 30 shock took 19.7 h to arrive at Earth and the sheath storm peaked within 7 h, which is ~3 h ahead of the MC arrival. SN MCs dominate in odd cycles such as the current one (23), so the delay time for most of the storms is smaller. Long delay times are expected for the even cycles (such as the coming cycle 24) because NS MCs dominate during those.

5. Source locations of CIR and CME storms

Only those IP structures that reach Earth have a chance to be geoeffective. To illustrate this, we have plotted the solar-source latitudes of intense (Dst $\leqslant -100$ nT) geomagnetic storms (see Zhang et al., 2007) during cycle 23 in Fig. 19. Storms caused by MCs, non-cloud ICMEs and CIRs are distinguished with different symbols. MC and non-cloud ICME storms will be referred to as CME storms. The solar sources of CIR storms are coronal holes. Both isolated coronal holes and equatorial extensions of polar coronal holes were responsible for the CIR storms. The CHs are generally more extended on the Sun, so it is somewhat

Please cite this article as: Gopalswamy, N., Solar connections of geoeffective magnetic structures. Journal of Atmospheric and Solar-Terrestrial Physics (2008), doi:10.1016/j.jastp.2008.06.010

difficult to define a heliographic location. For isolated coronal holes, the heliographic location corresponds to the centroid of the coronal holes. For equatorial extensions of polar holes, we have defined the heliographic location as the centroid of the CH area within a circle of 0.5 solar radii from the disk center when the CH is at the central meridian.

The number of intense storms is the least during the rise phase (15), with similar number in the maximum (32) and declining phases (33). However, the number of CME-related storms (32) peak in the maximum phase, with only 12 in the rise phase and 25 in the declining phase. Out of the 11 CIR storms, only 3 occurred during the rise phase and the remaining 8 occurred during the declining phase (none in the maximum phase). During the rise phase, all the CIR storms were due to isolated coronal holes, whereas in the declining phase, the CIR storms were due to both the equatorial extensions of polar holes and isolated low-latitude coronal holes.

One of the striking features of Fig. 19 is the confinement of the solar sources of major storms (both CME- and CH-related) to low latitudes ($\pm 30^\circ$) throughout the cycle. During the maximum and declining phases, the latitudes are much closer to the equator, as expected from the locations of active regions that form the butterfly diagram. Although CMEs originate from a wide range of latitudes during solar maxima, the ones causing geomagnetic storms are generally closer to the equator. There is one outlier in the rise phase (from S54E46), which may be the result of CME deflection towards the equator during the minimum phase when the global dipolar field of the Sun is very intense (Gopalswamy et al., 2000b; Filippov et al., 2001). The CME in question is a partial halo CME with a measured width of 174° and very slow (average speed within the coronagraphic field of view ~293 km/s). The source latitude inferred from the CME position angle (130°) is S40, compared to the source location at S54. This is a clear indication of equatorial deflection within the coronagraphic field of view (i.e., close to the Sun). Of course, there is always an element of uncertainty in CME source identifications: it is possible that this outlier may be a misidentification and the actual source may be closer to the equator, but was not detected by coronagraphs. CME deflection due to the global solar magnetic field has been proposed as one of the reasons for the unusually large number of MCs during solar minimum (Riley et al., 2006; Gopalswamy et al., 2008a).

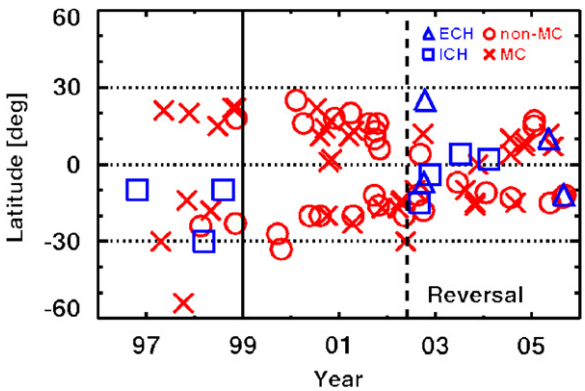

Fig. 19. Solar-source latitudes of large geomagnetic storms of solar cycle 23 plotted as a function of time. Storms due to MCs (crosses), non-cloud ICMEs (open circles) and CIRs (squares and triangles) are distinguished. CIR sources are further separated into those associated with isolated CHs (triangles) and equatorial extensions of polar CHs (squares). The solid vertical line (January 1999) divides the rise and maximum phases of cycle 23. The dashed vertical line (May 2002) divides the maximum and declining phases. Completion of the polarity reversal in both the poles marks the end of the maximum phase. MC-related storms (9) outnumber the CIR and non-cloud storms (3 each). No CIR storms occurred in the maximum phase, but there were 15 MC and 17 non-cloud storms. In the declining phase, the numbers remained high: 8 CIR, 14 MC and 11 non-cloud storms. The total number of intense storms is roughly the same in the maximum and declining phases being twice the number in the rise phase. CIR storms clearly dominate in the declining phase.

Combined with the fact that the longitude distribution of CMEs causing geomagnetic storms is generally centered close to the central meridian with a slight western bias (Wang et al., 2002; Zhang et al., 2003), we conclude that the source must be near the disk center whether it is a CME source region or coronal hole. However, Vrsnak et al. (2007b) studied the Dst variation during the 2005 and concluded that high-latitude coronal holes contribute to the Dst variation. The Dst values they considered are all above −60 nT (only two Dst values were below −50 nT) and hence do not qualify for intense storms we discussed in Fig. 19. Vrsnak et al. (2007b) obtained good correlation between Dst and solar wind speed ($r = 0.57$). However, for the intense CIR storms, we find a much weaker correlation between speed or speed-B products and Dst. The correlation coefficient is generally less than 0.3. The best correlation ($r = 0.50$) for the solar wind dynamic pressure and Dst.

Finally, we point out that there were only two major storms during the first year (1999) of solar maximum, both due to non-cloud ICMEs from the southern hemisphere. The overall impact of solar events (solar energetic particle events, IP type II bursts, and geomagnetic storms) were all low during 1999, which has not been fully understood (Gopalswamy et al., 2008b).

6. Summary and conclusions

We investigated the solar sources and geoeffectiveness of IP structures (ICMEs and CIRs). CMEs from active regions and fast solar wind from coronal holes are the near-Sun manifestations of these structures. On the visible solar-surface (photosphere), the CME sources correspond to regions of enhanced bipolar or mixed polarity regions, the enhancement being orders of magnitude higher than the quiet-Sun magnetic field values. A lot of magnetic energy can be stored in the corona above these active regions and released in the form of powerful CMEs. The average near-Sun speed of CMEs that cause intense geomagnetic storms exceeds 1000 km/s. The photospheric field in holes is also enhanced, but only by a factor of 2–3 compared to the quiet-Sun value; the field is also predominantly unipolar (open). The fast solar wind is accelerated and flows freely along the open field lines into

the IP medium. The fast wind finishes accelerating beyond ~10 solar radii from the Sun and interacts with the slow solar wind forming the interaction regions responsible for the geomagnetic storms. CMEs reach their peak speed within a few solar radii from the Sun and then propagate into the heliosphere, interacting with the surrounding solar wind (normally the slow solar wind). When fast enough, CMEs develop a shock, which is often observed at 1 AU and beyond. The sheath between CME flux rope and the shock can be considered as a structure similar to the interaction region due to the fast wind.

In the IP medium, there are several similarities between CIRs and CMEs. Both are magnetized structures with enhanced magnetic field, the enhancement above the quiet solar wind value being by a factor of 3–4. Both can drive shocks, although CIR shocks are formed only occasionally within 1 AU, while they are more common at a few AU from the Sun. Both CME and CIR shocks can accelerate energetic particles, but the intensity levels are much weaker for CIR shocks. The CIR particles reach their peak intensity at a distance of several AU from the Sun. On the other hand, energetic particles from CME-driven shocks are emitted from near the Sun to large distances into the heliosphere.

The geoeffectiveness of these structures depends on the magnetic field component pointing in the direction opposite to the horizontal field of Earth. The southward field inside ICMEs arises right at the Sun as a part of the eruption process. The southward field in sheaths can be as high as in flux ropes and comes from the outer corona and heliosphere overlying the eruption region. The sheath forms when the overlying plasma does not have enough time to flow around the flux rope. Although we have focused our attention mainly on the flux-rope structure (MC), non-cloud ejecta also occur frequently and can be geoeffective (see e.g., Borovsky and Denton, 2006; Georgieva et al., 2006).

As for CIRs, observing a coronal hole crossing the central meridian of the Sun is a good indicator of an impending HSS. The speed variability of HSS (from event to event) is only by a factor of 2, while for CMEs it can by an order of magnitude. There is active research to relate the speed of the fast wind to the properties of coronal holes not only in the corona, but all the way to the photosphere. Once there is a coronal hole, an interaction region almost always forms because of the neighboring quiet region to the west of the hole, which sends out slow wind. Depending on the relative speed, the fast wind collides with the slower one at some distance from the Sun. Alfvenic fluctuations are compressed due to the interaction and hence the magnetic field is enhanced in the CIR regions.

As for CME sheaths, it is surprising that the speed of CMEs correlate reasonably with the sheath magnetic field (better than that of the MC). Similarly, the Dst index also correlates well with the CME speed–sheath field product. There is some uncertainty as to what we observe as a CME near the Sun. The white-light coronagraphs simply measure a signature of the electron density, while at 1 AU a CME is predominantly recognized in magnetic field observations. The CME speed corresponds to the outermost visible feature, which could be a shock, sheath or compressed plasma. The problem is more complicated for Earth-directed CMEs (which cause geomagnetic storms) because the occulting disk of coronagraphs does not allow us to image the internal structure. The recently flown STEREO mission is expected to make progress on this issue because of the multiple views available for CMEs.

The solar sources of CMEs and CIRs are consistent with the requirement that they result in Earth-directed structures. While CMEs and coronal holes originate at all locations on the Sun, only those originating close to the solar disk center cause intense storms. As the solar source moves away from the Sun center, the likelihood of the structures originating from them reaching Earth diminishes because only the outer flanks are expected to encounter Earth. There may be additional factors that might send some CMEs towards Earth such as the global dipolar field during solar minimum and deflection by nearby coronal holes and CMEs.

For the ICME structure, our discussion was centered on the MCs not only because of the possibility that all ICMEs MCs, but also because of their connection to the solar magnetism in general. There is a specific 22-year pattern they follow in terms of the leading field observed in the IP medium. This might help us ultimately figure out how an ICME gets its sheath and cloud fields from the solar atmosphere. Predicting the strength and topology of the MCs based on solar remote sensing is a major challenge for the solar-terrestrial physics community. We have also used the term geoeffectiveness in a narrow sense of ring current enhancement measured by the Dst index. There are numerous other effects produced by the IP structures in the magnetosphere and various other layers down to the ground (see Borovsky and Denton, 2006; Miyoshi and Kataoka, 2008). ICMEs and CIRs make significantly different contributions to these effects.

Acknowledgments

The author thanks S. Yashiro, P. Mäkelä, and S. Akiyama for help with some figures. This article is based on an invited talk given at the 2007 AOGS meeting in Bangkok. This work was supported by NASA's LWS TR&T and SR&T programs. The author thanks the referees for constructive comments that helped improve the presentation of the paper.

References

Akasofu, S.-I., 1981. Energy coupling between the solar wind and the magnetosphere. Space Science Reviews 28, 121.

Belcher, L.W., Davis, J., 1971. Alfven wave in the interplanetary medium, 2. Journal of Geophysical Research 76, 3534.

Borovsky, J.E., Denton, M.H., 2006. Differences between CME-driven storms and CIR-driven storms. Journal of Geophysical Research 111, A07S08.

Bothmer, V., Schwenn, R., 1994. Eruptive prominences as sources of magnetic clouds in the solar wind. Space Science Reviews 70 (1–2), 215–220.

Brueckner, G.E., et al., 1995. The Large Angle Spectroscopic Coronagraph (LASCO). Solar Physics 162, 357–402.

Burlaga, L.F., 1995. Interplanetary Magnetohydrodynamics. Oxford University Press, New York.

Burlaga, L.F., Lepping, R.P., 1977. The causes of recurrent geomagnetic storms. Planetary and Space Science 25, 1151.

Burlaga, L.F., Klein, L., Sheeley Jr., N.R., Michels, D.J., Howard, R.A., Koomen, M.J., Schwenn, R., Rosenbauer, H., 1982. A magnetic cloud and a coronal mass ejection. Geophysical Research Letters 9, 1317–1320.

Burlaga, L.F., Skoug, R.M., Smith, C.W., Webb, D.F., Zurbuchen, T.H., Reinard, A., 2001. Fast ejecta during the ascending phase of solar cycle 23: ACE observations, 1998–1999. Journal of Geophysical Research 106, 20957–20978.

Chapman, S., Bartels, J., 1962. Geomagnetism, vol. 2. Clarendon Press, Oxford, pp. 541–1049.

Ciaravella, A., Raymond, J.C., Kahler, S.W., 2006. Ultraviolet properties of halo coronal mass ejections: doppler shifts, angles, shocks, and bulk morphology. Astrophysical Journal 652, 774.

Crooker, N.U., 2000. Solar and heliospheric geoeffective disturbances. Journal of Atmospheric and Solar Terrestrial Physics 62, 1071.

Dungey, J.W., 1961. Interplanetary magnetic field and the auroral zones. Physical Review Letters 6, 47.

Echer, E., Alves, M.V., Gonzalez, W.D., 2005. A statistical study of magnetic cloud parameters and geoeffectiveness. Journal of Atmospheric and Solar Terrestrial Physics 67, 839.

Filippov, B.P., Gopalswamy, N., Lozhechkin, A.V., 2001. Non-radial motion of eruptive filaments. Solar Physics 203, 119–130.

Fisk, L., Schwadron, N.A., Zurbuchen, T.H., 1999. Acceleration of the fast solar wind by the emergence of new magnetic flux. Journal of Geophysical Research 104, 19765–19772.

Fujiki, K., Hirano, M., Kojima, M., Tokumaru, M., Baba, D., Yamashita, M., Hakamada, K., 2005. Relation between solar wind velocity and properties of its source region. Advances in Space Research 35 (12), 2185–2188.

Georgieva, K., Kirov, B., Gavruseva, E., 2006. Geoeffectiveness of different solar drivers, and long-term variations of the correlation between sunspot and geomagnetic activity. Physics and Chemistry of the Earth 31, 81–87.

Gonzalez, W.D., Echer, E., 2005. A study on the peak Dst and peak negative Bz relationship during intense geomagnetic storms. Geophysical Research Letters 32, L18103.

Gonzalez, W.D., Clúa De Gonzalez, L., Dal Lago, A., Tsurutani, B.T., Arballo, J.K., Lakhina, G.S., Buti, B., Ho, G.M., 1998. Magnetic cloud field intensities and solar wind velocities. Geophysical Research Letters 25, 963–966.

Gonzalez, W.D., Tsurutani, B.T., Lepping, R.P., Schwenn, R., 2002. Interplanetary phenomena associated with very intense geomagnetic storms. Journal of Atmospheric and Solar Terrestrial Physics 64, 173–181.

Gonzalez, W.D., Clua-Gonzalez, A.L., Echer, E., Tsurutani, B.T., 2007. Interplanetary origin of intense geomagnetic storms (Dst <-100 nT) during solar cycle 23. Geophysical Research Letters 34, L06101.

Gopalswamy, N., 2002. Relation between CMEs and ICMEs. In: Wang, H.N., Xu, R.L. (Eds.), Solar-Terrestrial Magnetic Activity and Space Environment, COSPAR Colloquia Series, vol. 14, p. 157.

Gopalswamy, N., 2003. Coronal mass ejections: initiation and detection. Advances in Space Research 31, 869–881.

Gopalswamy, N., 2004. A global picture of CMEs in the inner heliosphere. In: Poletto, G., Suess, S. (Eds.), The Sun the Heliosphere as an Integrated System. Springer, New York, p. 201.

Gopalswamy, N., 2006a. Interplanetary coronal mass ejections. Space Science Reviews 124, 145–168.

Gopalswamy, N., 2006b. Coronal mass ejections and Type II radio bursts. In: Gopalswamy, N., Mewaldt, R., Torsti, J. (Eds.), AGU Monograph 165, Solar Eruptions and Energetic Particles, p. 207.

Gopalswamy, N., 2006c. Coronal Mass Ejections of Solar Cycle 23. Journal of Astrophysics and Astronomy 27, 243–254.

Gopalswamy, N., Shibasaki, K., Deforest, C. E., Bromage, B. J. I., Del Zanna, G., 1997. Multiwavelength Observations of a Coronal Hole. In: Balasubramaniam, K.S., Harvey, J., Rabin, D., (Eds.), Synoptic Solar Physics ASP Conference Series. Vol. 140, 1998, p. 363.

Gopalswamy, N., Shibasaki, K., Thompson, B.J., Gurman, J., DeForest, C., 1999a. Microwave enhancement and variability in the elephant's trunk coronal hole: comparison with SOHO observations. Journal of Geophysical Research 104, 9767–9780.

Gopalswamy, N., Shibasaki, K., Thompson, B.J., Gurman, J.B., Deforest, C.E., 1999b. Is the chromosphere hotter in coronal holes? In: Habbal, S.R., Esser, R., Hollweg, J.V., Isenberg, P.A. (Eds.), Solar Wind Nine. AIP Conference Proceedings, vol. 471, p. 277.

Gopalswamy, N., Lara, A., Lepping, R.P., Kaiser, M.L., Berdichevsky, D., St. Cyr, O.C., 2000a. Interplanetary acceleration of coronal mass ejections. Geophysical Research Letters 27, 145–148.

Gopalswamy, N., Hanaoka, Y., Hudson, H.S., 2000b. Structure and dynamics of the corona surrounding an eruptive prominence. Advances in Space Research 25 (9), 1851–1854.

Gopalswamy, N., Lara, A., Yashiro, S., Kaiser, M.L., Howard, R.A., 2001. Predicting the 1-AU arrival times of coronal mass ejections. Journal of Geophysical Research 106, 29207.

Gopalswamy, N., Lara, A., Yashiro, S., Howard, R.A., 2003. Coronal mass ejections and solar polarity reversal. Astrophysical Journal 598, L63–L66.

Gopalswamy, N., Yashiro, S., Michalek, G., Xie, H., Lepping, R.P., Howard, R.A., 2005a. Solar source of the largest geomagnetic storm of cycle 23. Geophysical Research Letters 32, L12S09.

Gopalswamy, N., Yashiro, S., Liu, Y., Michalek, G., Vourlidas, A., Kaiser, M.L., Howard, R.A., 2005b. Coronal mass ejections and other extreme characteristics of the 2003 October–November solar eruptions. Journal of Geophysical Research 110, A09S15.

Gopalswamy, N., Lara, A., Manoharan, P.K., Howard, R.A., 2005c. An empirical model to predict the 1-AU arrival of interplanetary shocks. Advances in Space Research 36 (12), 2289–2294.

Gopalswamy, N., Yashiro, S., Akiyama, S., 2007. Geoeffectiveness of halo coronal mass ejections. Journal of Geophysical Research 112, A06112.

Gopalswamy, N., Akiyama, S., Yashiro, S., Michalek, G., Lepping, R.P., 2008a. Solar sources and geospace consequences of interplanetary magnetic clouds observed during solar cycle 23. Journal of Atmospheric and Solar Terrestrial Physics 70, 245.

Gopalswamy, N., Yashiro, S., Xie, H., Akiyama, S., Aguilar-Rodriguez, E., Kaiser, M.L., Howard, R.A., Bougeret, J.L., 2008b. Radio quiet fast and wide coronal mass ejections. Astrophysical Journal 674, 560–569.

Gosling, J.T., Baker, D.N., Bame, S.J., Feldman, W.C., Zwickl, R.D., Smith, E.J., 1987. Bidirectional solar wind electron heat flux events. Journal of Geophysical Research 92, 8519–8535.

Gosling, J.T., Bame, S.J., McComas, D.J., Phillips, J.L., 1990. Coronal mass ejections and large geomagnetic storms. Geophysical Research Letters 127, 901–904.

Howard, R.A., Michels, D.J., Sheeley Jr., N.R., Koomen, M.J., 1982. The observation of a coronal transient directed at Earth. Astrophysical Journal 263, L101.

Huttunen, K.E.J., Schwenn, R., Bothmer, V., Koskinen, H.E.J., 2005. Properties and geoeffectiveness of magnetic clouds in the rising, maximum, and early declining phases of solar cycle 23. Annales Geophysicae 23, 625–641.

Kamide, Y., Yokoyama, N., Gonzalez, W., Tsurutani, B.T., Daglis, I.A., Brekke, A., Masuda, S., 1998. Two-step development of geomagnetic storms. Journal of Geophysical Research 103, 6917–6922.

Kataoka, R., Miyoshi, Y., 2006. Flux enhancement of radiation belt electrons during geomagnetic storms driven by coronal mass ejections and corotating interaction regions. Space Weather 4, S09004.

Kaymaz, Z., Siscoe, G., 2006. Field-line draping around ICMEs. Solar Physics 239, 437–448.

Kosugi, T., Ishiguro, M., Shibasaki, K., 1986. Polar-cap and coronal-hole-associated brightenings of the Sun at millimeter wavelengths. Publications of the Astronomical Society of Japan 38, 1–11.

Krieger, A.S., Timothy, A.F., Roelof, E.C., 1973. A Coronal hole and its identification as the source of a high velocity solar wind stream 1973. Solar Physics 29, 505–525.

Lepping, R.P., et al., 1995. The wind magnetic field investigation. Space Science Reviews 71, 207–229.

Lepping, R.P., Berdichevsky, D.B., Wu, C.-C., Szabo, A., Narock, T., Mariani, F., Lazarus, A.J., Quivers, A.J., 2006. A summary of WIND magnetic clouds for years 1995–2003: model-fitted parameters, associated errors and classifications. Annales Geophysicae 24 (1), 215.

Li, Y., Luhmann, J.G., 2004. Solar cycle control of the magnetic cloud polarity and the geoeffectiveness. Journal of Atmospheric and Solar Terrestrial Physics 66, 323.

Lindsay, G.M., Luhmann, J.G., Russell, C.T., Gosling, J.T., 1999. Relationships between coronal mass ejection speeds from coronagraph images and interplanetary characteristics of associated interplanetary coronal mass ejections. Journal of Geophysical Research 104, 12515–12524.

Loewe, C.A., Prolss, G.W., 1997. Classification and mean behavior of magnetic storms. Journal of Geophysical Research 102, 14209.

Lu, G., 2006. Geophysical Monograph 167, 97–111.

Malandraki, O.E., Lario, D., Lanzerotti, L.J., Sarris, E.T., Gerranios, A., Tsiropoula, G., 2005. October/November 2003 interplanetary coronal mass ejections: ACE/EPAM solar energetic particle observations. Journal of Geophysical Research 110, A09S06.

Marubashi, K., 1997. Interplanetary flux ropes and solar filaments. Geophysical Monograph 99, 147.

Please cite this article as: Gopalswamy, N., Solar connections of geoeffective magnetic structures. Journal of Atmospheric and Solar-Terrestrial Physics (2008), doi:10.1016/j.jastp.2008.06.010

McPherron, R.L., Weygand, J., 2006. Geophysical Monograph 167, 125–137.
Miyoshi, Y., Kataoka, R., 2005. Ring current ions and radiation belt electrons during geomagnetic storms driven by coronal mass ejections and corotating interaction regions. Geophysical Research Letters 32, L21105.
Miyoshi, Y., Kataoka, R., 2008. Flux enhancement of the outer radiation belt electrons after the arrival of stream interaction regions. Journal of Geophysical Research 113, A03S09.
Mulligan, T., Russell, C.T., Luhmann, J.G., 1998. Solar cycle variation of the structure of magnetic clouds in the inner heliosphere. Geophysical Research Letters 25, 2959.
Nolte, J.T., Krieger, A.S., Timothy, A.F., Gold, R.E., Roelof, E.C., Vaiana, G., Lazarus, A.J., Sullivan, J.D., Mclntosh, P.S., 1976. Coronal holes as sources of solar wind. Solar Physics 46, 303–322.
Owens, M.J., Cargill, P.J., Pagel, C., Siscoe, G.L., Crooker, N.U., 2005. Characteristic magnetic field and speed properties of interplanetary coronal mass ejections and their sheath regions. Journal of Geophysical Research 110, A01105.
Pulkkinen, T.I., Partamies, N., Huttunen, K.E.J., Reeves, G.D., Koskinen, H.E.J., 2007. Differences in geomagnetic storms driven by magnetic clouds and ICME sheath regions. Geophysical Research Letters 34, L02105.
Qiu, J., Hu, Q., Howard, T.A., Yurchyshyn, V.B., 2007. On the magnetic flux budget in low-corona magnetic reconnection and interplanetary coronal mass ejections. Astrophysical Journal 659, 758–772.
Riley, P., Schatzman, C., Cane, H.V., Richardson, I.G., Gopalswamy, N., 2006. On the rates of coronal mass ejections: remote solar and in situ observations. Astrophysical Journal 647, 648.
Schwenn, R., 2006. Solar wind sources and their variations over the solar cycle. Space Science Reviews 124, 51–76.
Sheeley Jr., N.R., Hakala, W.N., Wang, Y.-M., 2000. Detection of coronal mass ejection associated shock waves in the outer corona. Journal of Geophysical Research 105, 5081–5092.
Srivastava, N., Venkatakrishnan, P., 2004. Solar and interplanetary sources of geomagnetic storms during 1996–2002. Journal of Geophysical Research 109, A10103.
Tousey, R., 1973. The solar corona. Space Research 13, 713.
Tsurutani, B.T., Gonzalez, W.D., Gonzalez, A.L.C., Tang, F., Arballo, J.K., Okada, M., 1995. Interplanetary origin of geomagnetic activity in the declining phase of the solar cycle. Journal of Geophysical Research 100 (A11), 21717–21734.
Tsurutani, B.T., McPherron, R., Gonzalez, W., Lu, G., Sobral, J.H.A., Gopalswamy, N., 2006. Geophysical Monograph 167.
Tu, C.-Y., Zhou, C., Marsch, E., Xia, L.-D., Zhao, L., Wang, J.-X., Wilhelm, K., 2005. Solar wind origin in coronal funnels. Science 308 (5721), 519–523.
Turner, N., Mitchell, E.J., Knipp, D.J., Emery, B.A., 2006. Geophysical Monograph 167, 113–124.
Vrsnak, B., Zic, T., 2007. Transit times of interplanetary coronal mass ejections and the solar wind speed. Astronomy and Astrophysics 472, 937–943.
Vrsnak, B., Temmer, M., Veronig, A., 2007a. Coronal holes and solar wind high speed streams I: forecasting the solar wind parameters. Solar Physics 240, 315–330.
Vrsnak, B., Temmer, M., Veronig, A., 2007b. Coronal holes and solar wind high speed streams II: forecasting the geomagnetic effects. Solar Physics 240, 331–346.
Wang, Y.-M., Sheeley, N.R., 1990. Solar wind speed and coronal flux-tube expansion. Astrophysical Journal 355, 726–732.
Wang, Y.M., Ye, P.Z., Wang, S., Zhou, G.P., Wang, J.X., 2002. A statistical study on the geoeffectiveness of Earth-directed coronal mass ejections from March 1997 to December 2000. Journal of Geophysical Research 107 (SSH2-1).
Wu, C.-C., Lepping, R.P., 2002. Effect of solar wind velocity on magnetic cloud-associated magnetic storm intensity. Journal of Geophysical Research 107 (SSH3-1).
Yashiro, S., Gopalswamy, N., Michalek, G., St. Cyr, O.C., Plunkett, S.P., Rich, N.B., Howard, R.A., 2004. A catalog of white light coronal mass ejections observed by the SOHO spacecraft. Journal of Geophysical Research 109, A07105.
Yermolaev, Yu.I., Yermolaev, M.Yu., 2006. Statistical study on the geomagnetic storm effectiveness of solar and interplanetary events. Advances in Space Research 37 (6), 1175.
Yurchyshyn, V., Wang, H., Goode, P.R., Deng, Y., 2001. Orientation of the magnetic fields in interplanetary flux ropes and solar filaments. Astrophysical Journal 563, 381.
Yurchyshyn, V., Hu, C., Abramenko, V., 2004. Correlations between speeds of coronal mass ejections and the intensity of geomagnetic storms. Space Weather 2, S02001.
Zhang, J., Dere, K.P., Howard, R.A., Bothmer, V., 2003. Identification of solar sources of major geomagnetic storms between 1996 and 2000. Astrophysical Journal 582, 520–533.
Zhang, J., Liemohn, M.W., Kozyra, J.U., Lynch, B.J., Zurbuchen, T.H., 2004. A statistical study of the geoeffectiveness of magnetic clouds during high solar activity years. Journal of Geophysical Research 109, A09101.
Zhang, J., et al., 2007. Solar and interplanetary sources of major geomagnetic storms ($Dst \leqslant -100\,nT$) during 1996–2005. Journal of Geophysical Research 112, A10102.
Zhao, X.P., Webb, D.F., 2003. Source regions and storm effectiveness of frontside full halo coronal mass ejections. Journal of Geophysical Research 108, 1234.

Please cite this article as: Gopalswamy, N., Solar connections of geoeffective magnetic structures. Journal of Atmospheric and Solar-Terrestrial Physics (2008), doi:10.1016/j.jastp.2008.06.010